

# Quantifying plant-soil-nutrient dynamics in rangelands: Fusion of UAV hyperspectral-LiDAR, UAV multispectral-photogrammetry, and ground-based LiDAR-digital photography in a shrub-encroached desert grassland

Joel B. Sankey<sup>a,\*</sup>, Temuulen T. Sankey<sup>b,1</sup>, Junran Li<sup>c</sup>, Sujith Ravi<sup>d</sup>, Guan Wang<sup>c</sup>, Joshua Caster<sup>a</sup>, Alan Kasprak<sup>a,e</sup>

<sup>a</sup> Southwest Biological Science Center, Grand Canyon Monitoring and Research Center, U.S. Geological Survey, Flagstaff, AZ 86004, USA

<sup>b</sup> School of Informatics, Computing, and Cyber Systems, Northern Arizona University, 1295 S. Knoles Drive, Flagstaff, AZ 86011, USA

<sup>c</sup> Department of Geosciences, The University of Tulsa, Tulsa, OK 74104, USA

<sup>d</sup> Department of Earth and Environmental Science, Temple University, 1901 N. 13th Street, Philadelphia, PA 19122, USA

<sup>e</sup> Geosciences Department and Four Corners Water Center, Fort Lewis College, Durango, CO 81301, USA

## ARTICLE INFO

### Keywords:

Airborne data  
Drone  
Unmanned aerial system (UAS)  
Unmanned aerial vehicle (UAV)  
Terrestrial laser scanning  
Photogrammetry  
Structure from motion (SfM)  
Lidar  
Hyperspectral  
Machine learning  
Digital elevation model (DEM)  
Digital elevation model of difference (DOD)  
Change detection  
Rangeland  
Shrub  
Grass  
Soil  
Nutrient  
Fire  
Islands of fertility

## ABSTRACT

Rangelands cover 70% of the world's land surface, and provide critical ecosystem services of primary production, soil carbon storage, and nutrient cycling. These ecosystem services are governed by very fine-scale spatial patterning of soil carbon, nutrients, and plant species at the centimeter-to-meter scales, a phenomenon known as "islands of fertility". Such fine-scale dynamics are challenging to detect with most satellite and manned airborne platforms. Remote sensing from unmanned aerial vehicles (UAVs) provides an alternative option for detecting fine-scale soil nutrient and plant species changes in rangelands to smaller extents. We demonstrate that a model incorporating the fusion of UAV multispectral and structure-from-motion photogrammetry classifies plant functional types and bare soil cover with an overall accuracy of 95% in rangelands degraded by shrub encroachment and disturbed by fire. We further demonstrate that employing UAV hyperspectral and LiDAR fusion greatly improves upon these results by classifying 9 different plant species and soil fertility microsite types (SFMT) with an overall accuracy of 87%. Among them, creosote bush and black grama, the most important native species in the rangeland, have the highest producer's accuracies at 98% and 94%, respectively. The integration of UAV LiDAR-derived plant height differences was critical in these improvements. Finally, we use synthesis of the UAV datasets with ground-based LiDAR surveys and lab characterization of soils to estimate that the burned rangeland potentially lost 1474 kg/ha of C and 113 kg/ha of N owing to soil erosion processes during the first year after a prescribed fire. However, during the second-year post-fire, grass and plant-interspace SFMT functioned as net sinks for sediment and nutrients and gained approximately 175 kg/ha C and 14 kg/ha N, combined. These results provide important site-specific insight that is relevant to the 423 Mha of grasslands and shrublands that are burned globally each year. While fire, and specifically post-fire erosion, can degrade some rangelands, post-fire plant-soil-nutrient dynamics might provide a competitive advantage to grasses in rangelands degraded by shrub encroachment. These novel UAV and ground-based LiDAR remote sensing approaches thus provide important details towards more accurate accounting of the carbon and nutrients in the soil surface of rangelands.

## 1. Introduction

Rangelands cover approximately 70% of the global terrestrial land

surface (Holechek et al., 2011) and provide critical ecosystem services for 2 billion people (Briske, 2017). Rangelands also provide forage and water for 50% of the global livestock population, but are rapidly

\* Corresponding author at: N Gemini Drive, Flagstaff, AZ 86001, USA.

E-mail address: [jsankey@usgs.gov](mailto:jsankey@usgs.gov) (J.B. Sankey).

<sup>1</sup> J.B. Sankey and T.T. Sankey contributed equally to this manuscript

degrading due to changing climate, wildfire regimes, and economic policies that encourage land-use conversions (Briske, 2017). Monitoring rangeland biodiversity, health, and vegetation cover changes continues to be a high priority for resource managers around the world (Bradford et al., 2019; Millennium Ecosystem Assessment, 2005; UNCCD, 1994). However, rangeland monitoring can be expensive, time-consuming, and limited in spatial extent, since it is largely based on field measurements. Although field-based measurements provide detailed species-level information, extrapolating the species information over larger spatial extents with remote sensing data is challenging (Turner, 2014).

Rangelands around the world are commonly undergoing two major changes that alter the health and functioning of the ecosystems: shrub encroachment and fire disturbance (Archer et al., 2017; Barger et al., 2011; Van Auken, 2000). Several interacting climatic and anthropogenic factors are thought to contribute to shrub encroachment at local and regional scales including increase in aridity, fire intensity and frequency, grazing and browsing animals, and atmospheric CO<sub>2</sub> (Archer et al., 2017). Shrub encroachment reduces the herbaceous plant cover, forage, and diversity (Allred, 1996; Archer, 1996; Archer et al., 2017; Grover and Musick, 1990; Van Auken, 2000). Shrub encroachment can increase soil erosion and soil nutrient loss, and reduce soil carbon (C) and nitrogen (N) (Cunliffe et al., 2016b; Li et al., 2007, 2008; Miller et al., 2000; Puttock et al., 2014; Rau et al., 2009, 2011; Ravi et al., 2010; Schlesinger et al., 1990; Throop et al., 2013), because there is often not a 1:1 replacement of herbaceous cover by shrub cover, and because the erosive forces of wind and water are greater owing to fluid flow that is more channelized between shrubs compared to grasses and other herbaceous plants (Breshears et al., 2003; Lee et al., 1991a,b; Okin and Gillette, 2001; Okin, 2008; Ravi et al., 2010). In shrub-encroached grasslands, soil erosion occurs on unvegetated bare soil surfaces, while shrub and grass plant canopies intercept soil particles and adsorbed nutrients and accumulate them beneath the canopy (Cunliffe et al., 2016b; Dukes et al., 2018; Gonzales et al., 2018; Li et al., 2007, 2008; Ravi et al., 2019; Wang et al., 2019a, 2019b). Sub-canopy soil and nutrient accumulation lead to the formation of small “islands of fertility” that support plant growth, which in turn reinforces the fertile islands, while the unvegetated bare soil surfaces in the interspaces are further exposed to soil erosion and nutrient loss (Schlesinger et al., 1990, 1996).

To reduce these effects, intensive land treatments including prescribed burning, browsing, and mechanical and chemical removal of shrubs are commonly performed (Ravi et al., 2009; Ravi and D'Odorico, 2009; Van Wilgen and Trollope, 2003; White et al., 2006; White, 2011). Detecting shrub encroachment in grasslands with repeat images acquired from satellite sensors has not been widely feasible due to coarse spatial resolution (Huang et al., 2009; McGlynn and Okin, 2006; Strand et al., 2008; Washington Allen et al., 2006; Xian et al., 2015). Moreover, identifying the small islands of fertility (henceforth “soil fertility microsite types” or “SFMT”) based on spectral variability in soil texture, organic C, or nutrients, is complex and requires ground-based spectroradiometer data or airborne hyperspectral images (Angelopoulou et al., 2019; Crucil et al., 2019; Nocita et al., 2015; Van Cleemput et al., 2018; Waiser et al., 2007), which can be expensive to acquire. Tracking changes in erosion and deposition of soil, as well as the nutrients and organic C that are adsorbed to soil particles, requires highly accurate and precise topographic surveys (e.g., ground-based LiDAR; Eitel et al., 2011).

Newly available hyperspectral sensors aboard unmanned aerial vehicles (UAVs) provide a viable option to monitor rangelands at a local scale and at the individual plant canopy level (Kattenborn et al., 2019; Sankey et al., 2017a,b; Zhang et al., 2019). UAV hyperspectral remote sensing capabilities in rangeland SFMT mapping have not been tested and need to be evaluated given the widespread distribution of global rangelands thought to be a large terrestrial C pool (Abreu et al., 2017; Houghton, 2003; Pacala and Hurtt, 2001). Here we demonstrate UAV hyperspectral and LiDAR fusion in detecting the spatial patterning of shrubs, grasses, and soils associated with the small SFMT in burned and

unburned rangelands (Fig. 1).

Fire disturbance is common in rangelands, and fire regimes can change due to changing climate drivers and land use policies (Andela et al., 2019; Giglio et al., 2018; Hawbaker and Zhu, 2012). Both wild and prescribed fires provide a major disturbance that alters the plant species composition, biomass, aboveground and belowground C, and soil nutrients in rangelands (Wang et al., 2019a, 2019b). Post-fire C and nutrient pools are not commonly quantified with remote sensing methods in rangelands, especially compared to forested ecosystems (e.g., Kokaly et al., 2007; Miesel et al., 2018), despite their common occurrence and large impacts on the global terrestrial C and nutrient distribution. In shrub-encroached grasslands, post-fire soil erosion can occur on all bare soil surfaces but is especially pronounced on the SFMT that develop on raised microtopographic mounds of soil and plant litter beneath shrub and grass plant canopies (Dukes et al., 2018; Ravi et al., 2019; Sankey et al., 2012b; Wang et al., 2019a, 2019b). Owing to the post-fire erosion, the nutrient-rich soil patches are spatially redistributed, which resets the self-reinforcing feedbacks of shrub encroachment (Dukes et al., 2018; Wang et al., 2019a, 2019b). As a result, SFMT become more spatially homogenous after fire, and competitive advantages are hypothesized to become more evenly distributed for all plant functional cover types of shrubs and herbaceous species of grasses and forbs.

Plant-soil-nutrient dynamics in rangelands associated with ecological disturbance and changes in species composition are uniquely challenging for remote sensing (Cunliffe et al., 2016a; Duniway et al., 2012; Gillan et al., 2014; Lopatin et al., 2017; Solazzo et al., 2018; Sankey et al., 2019). First, rangeland plant species have low biomass and can be spectrally similar at wavelengths and bandwidths commonly employed in multispectral sensors (Okin et al., 2001), making it difficult to identify individual species within herbaceous or shrub functional cover types (Hunt, 2003; Ramsey et al., 2004; Sivanpillai and Booth, 2008). Multispectral satellite and airborne remote sensing applications in rangelands have, therefore, focused on separating grasslands from other common land cover types or on calculating vegetation indices as indicators of rangeland biomass and productivity. Species identification and biodiversity estimates are often accomplished with a handheld spectroradiometer at the leaf (Schweiger et al., 2018) and plot levels (Lopatin et al., 2017; Gholizadeh et al., 2019).

Second, rangeland plants and soils are often distributed in small patches (e.g., SFMT) that are less than a few square meters in dimension and are produced by fine-scale ecological and geomorphic processes. The small patches are difficult to identify, for example, in commonly available Landsat and MODIS satellite images with 900 m<sup>2</sup> and 2500 m<sup>2</sup> pixels, respectively, even with sub-pixel analysis (Sankey and Germino, 2008; Sankey et al., 2008b; Thomas and Ustin, 1987). In comparison, UAV images provide orders of magnitude finer spatial resolution at reasonable cost (Shin et al., 2018; Sankey et al., 2019). However, UAV multispectral images have not been widely applied in rangeland monitoring due to the challenges associated with distinguishing many spectrally similar species with a few spectral bands commonly available in UAV multispectral images (Colomina and Molina, 2014; Laliberte et al., 2011; Sankey et al., 2019).

Third, plant- and soil-nutrient dynamics are challenging and, in some cases, not currently feasible to estimate with remote sensing. While plant foliar nutrient content (Mitchell et al., 2012) and soil particle size, organic matter and nutrient content can be inferred from hyperspectral data, this is much more common via laboratory or in-situ spectroradiometer data (Angelopoulou et al., 2019; Brown et al., 2006; Nocita et al., 2015; Sankey et al., 2008; Waiser et al., 2007). Fourth, multispectral imagery often requires additional information about the relative height of plant canopies to accurately classify vegetation and soil. However, rangeland vegetation height only ranges between 20 cm and 5 m, which makes the application of airborne photogrammetry or LiDAR remote sensing challenging (Bork and Su, 2007; Cunliffe et al., 2016a; Gillan et al., 2014). Moreover, soil erosion and deposition in rangelands can

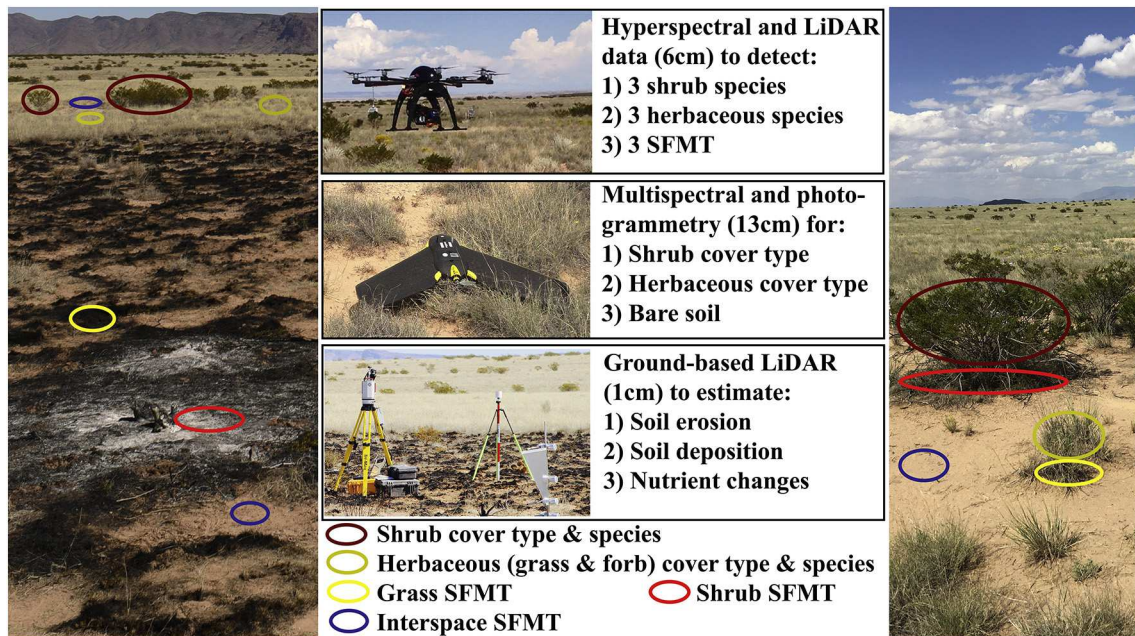


**Fig. 1.** UAV hyperspectral, multispectral, photogrammetry, and LiDAR as well as ground-based LiDAR remote sensing tools used in this study to examine the spatial patterning of shrubs, grasses, and soil associated with small “islands of fertility” ubiquitous in burned and unburned rangelands (sensu Schlesinger et al., 1996; termed “soil fertility microsite types” or “SFMT” in this paper).

produce very small elevation changes of only 1–2 cm (White, 2011). The small cm-scale changes that can occur as a result of ecological disturbance in rangelands specifically require tools such as survey-grade ground-based LiDAR or other land-surveying tools that can come with a high financial cost and learning curve for users (Eitel et al., 2011; Sankey et al., 2012a; Gillan et al., 2016; Kasprak et al., 2019).

Owing to those remote sensing challenges, it is not logistically feasible to implement a comprehensive rangeland monitoring protocol over large spatial extents that encompasses soil texture, water, nutrients, and plant species structure, function, and competitive interactions in many management scenarios. However, it is possible to track many of the key dynamics and feedbacks that shape rangeland ecosystems via high spatial and spectral resolution remote sensing.

### 1.1. Objectives

We use UAV hyperspectral, LiDAR, and multispectral sensors with ground-based LiDAR and real-time kinematic global positioning system (RTK-GPS) surveys to estimate changes in rangeland plant functional groups, plant species, and soil composition (Fig. 1) at the fine spatial extent of SFMT where nutrients and C accumulate at the soil surface, following fire disturbance in a grassland degraded by shrub encroachment. Such changes and dynamics have not been well-quantified previously via manned airborne or satellite data due to their coarse spatial resolution despite the widespread distribution of global rangelands.

Specifically, our objectives are to:

1. Map plant functional cover types, plant species composition, and SFMT in adjacent burned and unburned shrub-encroached grasslands and determine whether changes in source and sink dynamics of sediment and nutrients can be accurately monitored annually by quantifying soil erosion and deposition within the burned SFMT;
2. Determine the added value of using height information about SFMT and plants in combination with spectral data, specifically investigating the strengths and weaknesses of UAV hyperspectral-LiDAR fusion at relatively higher spatial resolution vs. UAV multispectral-photogrammetry fusion at comparatively lower spatial resolution available at a more affordable cost.

## 2. Methods

### 2.1. Rangeland site description

This study was conducted at the Sevilleta Long-Term Ecological Research (LTER) rangeland located 42 km NE of Socorro, New Mexico, USA (Fig. 2). The Sevilleta LTER is operated by the University of New Mexico and is located within the Sevilleta National Wildlife Refuge (SNWR), which is managed by the US Fish and Wildlife Service (USFWS). The climate consists of hot summers (ranging on average from 16 to 35 °C) and cool winters (−3 to 16 °C), with 260 mm of annual rainfall on average that predominantly falls during the June–September summer Monsoon season. Within the LTER and SNWR, our study focuses on an ecotone of black grama (*Bouteloua eriopoda*)-dominated grassland encroached by creosote bush (*Larrea tridentata*) shrubs in the northern Chihuahuan Desert biome. The geomorphic setting of the shrub-grassland ecotone is a nearly flat piedmont in the Rio Grande river valley at an average elevation of 1595 m. Soils are generally sandy loam texture. However, texture, nutrient, C, and moisture characteristics of the soil surface vary spatially at the patch scale of shrub, grass (herbaceous), and plant-interspace (i.e., unvegetated or mostly bare) SFMT (Cunliffe et al., 2016b). This spatial variability comprises “islands of fertility” that are similarly found in desert, grass, and shrub rangelands around the world (Schlesinger et al., 1996). The shrub and grass SFMT are microtopographic mounds that are 0.1–1 m higher in elevation, and accumulate and store soil C and N in concentrations 2–3 times greater, relative to adjacent unvegetated, interspace SFMT (Sankey et al., 2012a; Wang et al., 2019a, 2019b). In contrast, the interspace SFMT are unvegetated microtopographic depressions that are continuously exposed to water and wind erosion and, therefore, contain lesser amounts of soil C, N, and other nutrients.

The USFWS uses prescribed fires on a sub-decadal reburn interval to counter shrub-encroachment and maintain the health of this grassland ecosystem, which is used by pronghorn antelope and other wild ungulates for grazing and forage. On March 10, 2016, the USFWS conducted a 1-ha prescribed fire and a multi-year study ensued to monitor the plant-soil-nutrient feedbacks in the intentionally disturbed shrub-encroached grassland (Fig. 2). Published results from field- and lab-



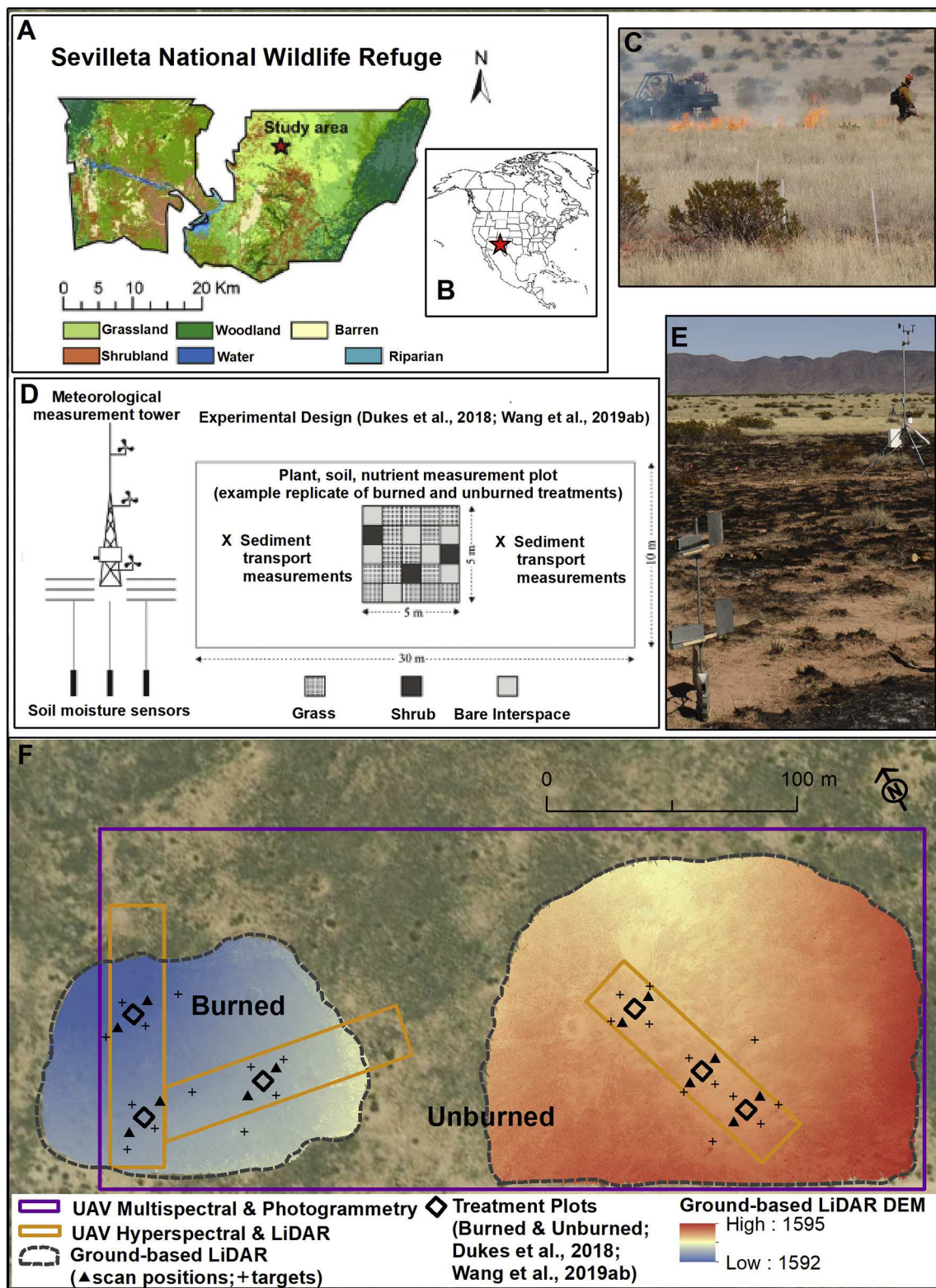


**Fig. 2.** Location of the study site within (A) Sevilleta National Wildlife Refuge, and (B) North America. A prescribed fire (C) was conducted in 2016 and study plots and equipment were installed (D, E; (Dukes et al., 2018; Wang et al., 2019a,b)) to examine the effects of burning for plant-soil-nutrient feedbacks at the scale of soil fertility microsite types (SFMT) in the shrub-encroached grassland. (F) Ground-based LiDAR surveys were repeatedly conducted one week, one year, and two years after the prescribed fire. (F) UAV data were acquired six months after the fire. In (F) the background imagery is from the National Agriculture Imagery Program (NAIP).

based monitoring during the study indicated significantly different soil C and N storage in the undisturbed compared to intentionally disturbed rangeland (Dukes et al., 2018; Gonzales et al., 2018; Ravi et al., 2019; Wang et al., 2019a, 2019b). Specifically, the undisturbed shrub SFMT contained significantly greater C, N and other nutrients compared to the grass SFMT, which in turn maintained greater concentrations relative to the interspace SFMT. The shrub SFMT also maintained coarser soil textures and higher soil water content after rainstorms compared to the grass and interspace SFMT (Gonzales et al., 2018). However, disturbance by fire and subsequent accelerated sediment transport redistributed soil particles and adsorbed nutrients, resulting in a more spatially homogeneous and equal distribution of these properties among the three SFMT types and resulting in lower soil water content following rainstorms on the shrub SFMT. These changes suggest that the intentional disturbance by burning lessened the competitive advantages of shrubs relative to grasses (Dukes et al., 2018; Gonzales et al., 2018; Wang et al., 2019a, 2019b). At the beginning of the experiment in 2016, we initiated acquisition of high-resolution remote sensing data of the fine-scale plant and soil variables. Ground-based lidar surveys were repeatedly conducted one week, one year, and two years after the prescribed fire. All UAV data were acquired six months after the prescribed fire.







## 2.2. Data acquisition

### 2.2.1. Ground-based observations to guide training pixel selection

On September 2 and 3, 2016, we mapped the locations of individual plants and SFMT on the ground across our image extents and within study plots in burned and unburned areas shown in Fig. 2 (E&F) to guide our selection of training and validation pixels for image analyses. We used a TOPCON GR3 RTK-GPS rover and base station located on a recorded monument. The estimated survey precision based on repeat survey of control points on fixed monuments was 0.010, 0.007, and 0.005 m in the Easting, Northing, and elevation dimensions, respectively. Point coordinates were recorded in UTM NAD83 (2011) Zone 13 N. Using the rover on a fixed-height rod to survey the coordinates of the center of individual shrubs, forbs, bunches of grasses, and SFMT, we mapped locations of the dominant plant species and SFMT as 9 target cover types (Table 1). These included the following dominant plant species: creosote bush (*Larrea tridentata*), four-wing saltbush (*Atriplex canescens*), ephedra (*Ephedra* species), and black grama (*Bouteloua eriopoda*). Another grass species, *Muhlenbergia arenicola*, was less abundant and was grouped with additional, even less common undifferentiated grass species in a single class termed “other grasses”. Similarly, we mapped forb species as a single, combined class termed “common forbs”, which included various genera and species from the *Asteraceae* family

**Table 1**

Cover types and number of individuals mapped in the field. These individuals were used to guide the selection of pixels from the imagery to develop training and validation sample sets detailed in Tables 3 and 4. Figs. 1 and 3 show examples and spectral reflectance of these cover types, respectively.

ID#	Cover Type	Functional Cover Type	Individuals Mapped (total N = 38)	Example Photo
1	Interspace soil SFMT	Bare Soil	3	See Fig. 1
2	Grass soil SFMT	Bare Soil	3	See Fig. 1
3	Shrub soil SFMT	Bare Soil	4	See Fig. 1
4	Black grama ( <i>Bouteloua eriopoda</i> )	Herbaceous	3	
5	Other grasses (e.g. <i>Muhlenbergia arenicola</i> )	Herbaceous	2	
6	Common forbs (e.g., <i>Asteraceae</i> species)	Herbaceous	8	
7	Four-wing saltbush ( <i>Atriplex canescens</i> )	Shrub	6	
8	Creosote bush ( <i>Larrea tridentata</i> )	Shrub	6	
9	Ephedra ( <i>Ephedra</i> species)	Shrub	3	
10	Shadow	—	—	—

with green leaves and white, yellow, or purple flowers at the time of the image acquisition. We also mapped locations of the three SFMT types where they were bare and not covered by a plant canopy: 1) nutrient-rich shrub SFMT, 2) nutrient-rich grass SFMT, and 3) nutrient-poor interspace SFMT. The study plots located within the burned and unburned areas were 5 m × 5 m (Fig. 2) and had been installed immediately prior to the fire by Dukes et al. (2018) and Wang et al. (2019a, 2019b) to monitor changes in the spatial distribution of plants, soil, nutrients, and water.

In the various image datasets used in this study, each individual mapped plant or SFMT is represented by numerous pixels (e.g., 10s to 100 s of pixels). Thus, we used the mapped individuals to guide the selection of pixels from the imagery to develop training and validation sample sets described in later sections of the methods below. Specifically owing to the high spatial resolution of the hyperspectral UAV data, we added shadow as a 10th class as described below, which we did not map on the ground.

### 2.2.2. Ground-based LiDAR surveys

On March 11, 2016, we conducted ground-based LiDAR surveys of the entire 1-ha burned area and adjacent unburned rangeland (Fig. 2). We used a Riegl VZ-1000 scanner to measure the horizontal coordinates, elevation, and near-infrared intensity of each LiDAR return (RIEGL, 2017). We used a calibrated Nikon D810 digital camera mounted on the scanner to assign red-green-blue (RGB) DN values to each LiDAR return from co-registered photos (RIEGL, 2017). The scanner has a beam divergence of 0.3 mrad, yielding laser pulse footprints of <2 mm at 3 m range. The manufacturer-quoted one-sigma precision and accuracy of the laser are 5 mm and 8 mm, respectively, at 100 m range. We collected data at a pulse repetition rate of 300 kHz using a 360 degree horizontal field of view and a 100 degree vertical field of view (30–130 degrees), with 90 degrees representing the central plane and 0 degrees representing the zenith. We performed scans at an angular resolution of 0.04 × 0.04 degrees from six scan positions adjacent to three study plots within the burned area, and from six scan positions adjacent to 3 study plots within the unburned rangeland. At each plot, one scan position was located on the NE edge and one was located on the SW edge (Fig. 2F). An additional detailed higher-resolution scan was acquired of the plot extent from each scan position, at an angular resolution of 0.02 × 0.02 degrees, constrained to a narrow field of view that only encompassed the study plot.

The data were registered between scans and scan positions using six reflective targets located on survey tripods and six reflective targets located on rebar points in the burned rangeland that did not change position throughout the study; the same approach was used in the unburned rangeland. The geolocation of each reflective target was determined with an RTK-GPS survey with a TOPCON GR3 rover and a base station located on a recorded monument. Reflective target coordinates were recorded in UTM NAD83 (2011) Zone 13 N and used to georeference two datasets: one coregistered dataset for the burned rangeland and another for the unburned rangeland. In March of 2017 and 2018, ground-based LiDAR surveys were conducted using identical methods as described for 2016. However, instead of georeferencing the 2017 and 2018 LiDAR datasets with RTK-GPS surveys, we directly registered each

of the later datasets to the georeferenced 2016 dataset using the reflective targets located on the rebar points that did not change position throughout the study (Table 2). The final coregistered and georeferenced dataset in the burned rangeland had a mean (standard deviation) point density within the small study plots of 10 (4) points/cm<sup>2</sup>. All the above data processing steps were conducted in Riegl RiscanPro software v. 2.6.2.

### 2.2.3. Fixed-wing UAV flight

We flew a Sensefly eBee AG fixed-wing UAV platform (Sensefly, Lausanne, Switzerland) on September 3, 2016. We used a multispectral (multiSPEC4C) sensor (maximum f/# = 1.8) with four spectral bands: green (550 nm band center), red (660 nm), red edge (735 nm), and near-infrared (790 nm). A single flight was performed close to solar noon at 80 m altitude above ground with 80% and 90% latitudinal and longitudinal overlap, respectively, which resulted in image pixel resolution of 13 cm. The flight lasted ~32 min covering 4.15 ha of burned and unburned rangeland (Fig. 2) with a total of 288 images in each of the four spectral bands. The flight mission planning, execution, and control via a wireless transmitter were implemented in Sensefly eMotion software (Sensefly, Lausanne, Switzerland). During the flight, each image was tagged with GPS coordinates (Easting, Northing, and elevation) recorded by the onboard gyroscopic sensor as well as the roll, pitch, and yaw of the aircraft relative to the coordinates.

### 2.2.4. Octocopter UAV flights

We performed three flights with a multirotor UAV platform on September 2, 2016 over targeted sections totaling 0.54 ha (Fig. 2) of the extent imaged by the fixed-wing UAV multispectral sensor that contained the burned and unburned rangeland and the experimental study plots surveyed with ground-based LiDAR. Each flight lasted for ~6 min. Developed to carry a heavy sensor payload, the octocopter UAV weighs 5.5 kg (Service-Drone, Germany) and flies for a maximum of ~9 min, a shorter period compared to the fixed-wing UAV, owing to the limitations in the current battery capabilities. The octocopter UAV is controlled via a hand-held remote transmitter and a ground control station, which sends waypoint navigation information to the aircraft from a laptop computer and the GroundStation software (Service-Drone, Germany), in which the flight path, direction, altitude, and speed are defined by the user and then transmitted to the UAV. We flew the octocopter UAV at 50 m altitude above ground for all three flights close to solar noon with wind speed of <3 m/s. The platform is stable in windy conditions up to 15 m/s.

The octocopter UAV carries aboard an inertial navigation system (INS), a LiDAR scanner, a hyperspectral sensor, and a data storage unit, all integrated on a single 3-axis gimbal. The INS has an integrated survey-grade Global Navigation Satellite System (GNSS) receiver and an inertial motion unit (IMU) that correct for errors associated with pitch, roll, and heading (0.05°, 0.05° and 0.5° RMS, respectively; SBG Systems North America, Inc., Chicago, IL). The hyperspectral pushbroom sensor (f/# = 2.5) covers the 400–1000 nm spectral range in 272 bands and is radiometrically calibrated by the manufacturer (Nano-Hyperspec sensor, Headwall Photonics Inc., Fitchburg, MA). Our flight speed and altitude at 50 m above ground resulted in the targeted image spatial

**Table 2**  
Registration statistics for georeferencing of ground-based LiDAR datasets.

Treatment	Year	Registration reference	Registration RMSE (m)			
			Overall	Easting (X)	Northing (Y)	Elevation (Z)
Burned	1 (2016)	Targets georeferenced w/ RTK-GPS to UTM NAD83 (2011) Zone 13 N	0.0094	0.0003	0.0087	0.0025
	2 (2017)	Targets georeferenced to 2016 dataset	0.0107	0.0052	0.0001	0.0025
	3 (2018)	Targets georeferenced to 2016 dataset	0.0094	0.0042	0.0002	0.0027
Unburned	1 (2016)	Targets georeferenced w/ RTK-GPS to UTM NAD83 (2011) Zone 13 N	0.0100	0.0003	0.0103	0.0001
	2 (2017)	Targets georeferenced to 2016 dataset	0.0019	0.0005	0.0001	0.0002
	3 (2018)	Targets georeferenced to 2016 dataset	0.0032	0.0009	0.0001	0.0008



extent of  $15 \text{ m} \times 120 \text{ m}$  ( $1,800 \text{ m}^2$ ) per flight and a spatial resolution of 6 cm for the 272 spectral bands.

The LiDAR on the octocopter UAV is a Velodyne HDL-32E LiDAR scanner integrated with the onboard data storage and GNSS INS/IMU. The LiDAR scanner employs 32 laser beams and  $40^\circ$  field of view as it rotates  $360^\circ$  at a  $100^\circ$  angle on the gimbal (Sankey et al., 2017a, 2017b) with  $\pm 2 \text{ cm}$  accuracy (Velodyne Acoustics, Inc., Morgan Hill, CA). The lasers have a wavelength of 903 nm and a max range of 80–100 m. The sensor has a 10 Hz frame rate, horizontal angular resolution of 0.16 degrees at 600 rpm, and a vertical angular resolution of 1.33 degrees. The resulting point density is dependent on flight speed. At an average flight speed of 3 m/s, the three flights with the octocopter UAV produced a mean LiDAR point density of 200 points/ $\text{m}^2$ . When the sensors are operated simultaneously, as in this study, the returned LiDAR data extent is slightly smaller than the hyperspectral.

## 2.3. Data pre-processing

### 2.3.1. 3D point cloud generation

**2.3.1.1. Ground-based LiDAR point cloud data pre-processing.** The georeferenced and co-registered ground-based LiDAR point cloud datasets were classified into vegetation and bare earth returns using the height-filtering methods of the BCAL LiDAR toolkit (<http://bcal.geology.isu.edu/tools-2/envi-tools>) which are described in detail by Glenn et al. (2006) and Streutker and Glenn (2006) and were previously evaluated at our study site by Sankey et al. (2012a). In brief, the height filtering process employs an initial estimate of canopy spacing to identify high-confidence ground points which are interpolated to generate a representation of the ground surface upon which all points are classified as either ground or vegetation. For the height filtering we specified required user-defined parameters of: 100 iterations, linear interpolation, 0.01 m vertical threshold, and 0.02 m canopy spacing. We visually inspected the classification output and repeated the process as necessary to ensure, for example, that short vegetation was not mistaken for the soil surface in the final classification. DEMs of the bare soil surface were generated at 0.01-m pixel resolution from the classified ground returns for 2016, 2017, and 2018, respectively. In the DEMs, elevation values for pixels that lacked one or more corresponding classified ground returns were not interpolated from surrounding pixels and were instead coded as “no data”. In the DEMs of the burned but vegetated plots (i.e., not including those acquired one-week post-fire) pixels coded as no data accounted for 28–58% of the total DEM cells. The 2016 and 2017, as well as the 2017 and 2018 DEMs were differenced to produce two Digital Elevation Models of Difference (DODs) that quantify topographic changes within the study area due to soil erosion and deposition. The above processing steps were conducted for the burned and unburned control plots of the study area. For the control plots, however, owing to the greater vegetation cover and very high 0.01-m pixel resolution of the DEMs, we only evaluated topographic changes in unvegetated, and thus interspace SFMT portions of the DODs. All the above data processing steps were conducted in ENVI 5.0. software (Harris Geospatial, Boulder, CO).

**2.3.1.2. Fixed-wing UAV photogrammetry point cloud data pre-processing.** Post flight, we used the eMotion software to integrate each geo-tagged image with the GPS coordinates. We photogrammetrically generated 3-D point cloud data using all the individual images (a methodology that is also commonly termed structure-from-motion or SfM) in the Pix4D software, which used the GPS coordinates and 3710 tie-points within the images to georeference and co-register the 3D data. A separate 3D point cloud was generated for each spectral band and we merged the four datasets to create a single, dense point cloud. The resulting average point density was  $>115 \text{ points/m}^2$ . The final merged and orthomosaicked images from the fixed-wing UAV had a root mean

squared error (RMSE) of 1.8 m, 1.6 m, and 2.9 m, respectively, for the geolocation errors (calculated as the difference between camera initial geolocations and their computed positions) in the Easting, Northing, and elevation dimensions. Comparison of 212,000 tie points (e.g., from unchanging objects such as rock, signs and other science infrastructure at the LTER; see Fig. 2) using the Cloud-to-Cloud registration tool in CloudCompare software, indicated that this point cloud can be directly registered (via translation and rotation in each dimension) to the 2016 ground-based LiDAR survey with a resulting total RMSE of 0.04 m among the Easting, Northing, and elevation.

Using the 3-D point cloud data in ENVI 5.2 software with the BCAL LiDAR toolkit (<http://bcal.geology.isu.edu/tools-2/envi-tools>; Glenn et al., 2006; Streutker and Glenn, 2006); we classified ground versus vegetation returns in the same way as described above for ground-based lidar data but using different parameters of: 15 iterations, linear interpolation, 0.01 m vertical threshold, and 5 m canopy spacing. In the resulting vegetation point cloud, the mean and maximum plant heights were calculated and summarized in 13 cm cells, consistent with the pixel size of the multispectral data (described below).

**2.3.1.3. Octocopter UAV LiDAR point cloud data pre-processing.** The octocopter UAV LiDAR data were pre-processed in the HyperspecIII software (Headwall Photonics Inc., Fitchburg, MA), which geometrically corrects the LiDAR data using GPS and IMU measurements and associated offsets (in degrees) for roll, pitch, heading, timing, and altitude. Next, the UAV LiDAR point cloud from each flight was directly registered to the georeferenced ground-based Riegl VZ-1000 LiDAR point cloud acquired in 2016. We performed the registration for each point cloud from the three flights using 21,000–27,000 tie points (e.g., from unchanging objects such as rock, signs and other science infrastructure at the LTER; see Fig. 2) and the Cloud-to-Cloud registration tool in CloudCompare software with resulting total RMSE of 0.015–0.018 m among the Easting, Northing, and elevation dimensions.

We classified the LiDAR point cloud into ground versus vegetation returns using ENVI 5.2 software with the BCAL LiDAR toolkit with a natural neighbor interpolation, which replaces empty cells with the neighboring classified returns. We summarized the classified point cloud in 6 cm raster cells, consistent with the hyperspectral image spatial resolution. Specifically, we summarized: 1) minimum, 2) mean, and 3) maximum ground surface elevation values; 4) minimum, 5) mean, and 6) maximum plant height values; and (7) standard deviation of plant height values inside each 6 cm cell. All pixels were classified in each raster, and those pixels that lack vegetation have values of 0 in the plant height rasters.

### 2.3.2. Generation of multispectral and hyperspectral images

**2.3.2.1. Generation of multispectral images.** We used Pix4D software to co-register all images to create a single orthomosaicked image for each spectral band based on the median spectral values per pixel for all calibrated images used in the mosaic. In the production of the orthomosaic, filtering based on image sharpness was used to exclude motion-blurred images. The resulting four spectral bands were layer stacked to create a single, multispectral image covering the entire 4.15 ha extent.

**2.3.2.2. Generation of hyperspectral images.** The hyperspectral images were acquired in individual tiles, which were georeferenced using the SpectralView software (Headwall Photonics Inc., Fitchburg, MA) with the GPS and IMU data for roll, pitch, and heading as well as altitude, flight direction, and timestamps acquired from the flight log and metadata (Sankey et al., 2017a, 2017b). In the SpectralView software, the hyperspectral images were also orthorectified using a US Geological Survey (USGS) digital elevation model (DEM) at 10 m spatial resolution as a baseline elevation dataset. The hyperspectral image tiles were then mosaicked in ENVI 5.2 and registered to the georeferenced UAV LiDAR

data (which had been registered to the ground-based LiDAR data acquired in 2016 as described above). The final hyperspectral image nominal registration errors relative to the UAV LiDAR were 0.001 m and 0.180 m in the Easting and Northing dimensions. We converted the orthomosaicked hyperspectral image from calibrated radiance to reflectance using the maximum radiance values in the UAV hyperspectral data from ground-based, black-and-white checkerboard calibration reflectance targets (Sankey et al., 2017a) and by dividing each calibrated radiance value for each pixel by the maximum radiance values in the respective spectral band.

## 2.4. Image classification

### 2.4.1. Classification of digital photos acquired during ground-based LiDAR surveys

The co-registered digital photos acquired during the ground-based LiDAR survey in 2016 were mosaicked into a single image for each of three 5 m × 5 m monitoring plots burned by the prescribed fire using Riegl RiscanPro software v. 2.6.2. The three mosaics were then classified into the three soil SFMT types of burned shrub, burned grass, or interspace soil, using the deep convolutional neural network method published by Buscombe and Ritchie (2018) and implemented in Python. In brief, the machine learning method uses fully-connected conditional random fields to probabilistically predict pixel classes based on supervision derived from training images that are visually inspected by the image analyst and labelled by landcover class. For this application, an independent set of 3 images (one of each plot and different photos than those used to generate the mosaics that were classified) were labelled and used for training; we heuristically adjusted the model parameters until the training classification output was visually satisfactory; then we applied the model to the three mosaics to produce the final classifications for each plot. The machine learning approach was methodologically useful for automating an otherwise more laborious process of manually delineating (i.e., digitizing) the boundaries between individual SFMT cover types in the images. We evaluated the accuracy of the classifications in two ways: 1) we quantitatively compared them to the ground-based observation locations of individual SFMT acquired for image analyses (Table 1) and determined that they correctly identified all individual SFMT surveyed within the plots (i.e., total classification accuracy = 100%); 2) we qualitatively assessed the classifications visually and determined that they were extremely consistent with photos in which we manually delineated (digitized) the boundaries between individuals of the three SFMT cover types. The classified mosaics were then imported into the 2016 ground-based LiDAR project in RiscanPro and used to classify the bare earth points by SFMT. The classified point cloud for each plot was then gridded in ENVI 5.0 to produce a 1-cm resolution raster classification map of the distribution of SFMT within each plot in 2016, one day after the prescribed fire.

### 2.4.2. Classification of imagery acquired from UAVs

**2.4.2.1. Fixed-wing UAV multispectral and photogrammetry data classification.** We layer-stacked the mean and maximum plant height raster bands derived from the fixed-wing photogrammetry point cloud with the four spectral bands of the multispectral orthomosaic to create a final image with six bands for classification. Since the fixed-wing UAV multispectral data included only four spectral bands, we added the plant height information to aid in classifying the rangeland cover types. Shrubs in the burned and unburned rangeland had an average canopy height of >40 cm, which was important in distinguishing them from considerably shorter herbaceous plant cover types and bare ground. The final 6-band multispectral and canopy height image was classified using classification and regression tree (CART) analysis (Breiman, 1984; Lawrence and Wright, 2001) in ENVI 5.2 software (Harris Geospatial, Boulder, CO, USA). Predictive CART models with recursive binary

splitting were developed in R software (version 3.5.3; 'rpart' package). CART was chosen due to its simplicity, widespread use, the automated weighing of the importance of the input variables, and flexibility with non-linear and non-parametric data (Breiman, 1984; Lawrence and Wright, 2001). Our preliminary analyses also indicated that CART produced much more accurate results than other common supervised classification models that integrated all available bands with equal weights of importance. Once the final predictive models were developed, they were implemented in ENVI 5.2 using the decision tree classifier to classify the image.

We evaluated two separate classifications developed with CART, namely a functional cover type classification and a species level classification that also included SFMT. The cover types classified in each classification are listed in Table 1. The functional cover type classification mapped total shrub, herbaceous, and bare soil cover. We additionally implemented the classification at the species level to determine if the fixed-wing UAV multispectral image with 13 cm resolution can be used to accurately map the more detailed cover types. Our goal was to determine if the more affordable fixed-wing UAV dataset could be used to classify the functional cover types as well as the rangeland species and SFMT in burned and unburned rangelands, or if the multispectral image had detection limits in rangeland applications that can be quantified despite its very high spatial resolution.

Independent sets of training and validation pixels were used to produce and assess the functional cover classification; the sample sizes are listed in Table 3. The same training and validation pixels (Table 3) were also used to produce and assess the species-level classification. Given the additional detail of plant species or SFMT identified, the species-level classification included 21–212 individual pixels for each cover type in the training and validation datasets. We assessed the user's (corresponding to errors of commission), producer's (corresponding to errors of omission), and overall accuracies of each classification (Congalton and Green, 2002; Olofsson et al., 2014). Rather than the kappa statistic, we calculated these accuracies using a full confusion matrix with the validation pixels (Table 3) to directly compare the accuracies of the two classifications (Congalton and Green, 2002; Foody, 2002; Olofsson et al., 2014).

Based on the importance values of the input data, the final CART models for plant species and functional cover types used 5 of the 6 bands: red, red edge, NIR spectral bands, and the mean and maximum plant height bands. Importantly, a mean plant height threshold of 42 cm was selected in the functional cover type model as a critical binary split between shrubs versus other cover types. The maximum plant height band was selected to separate some of the plant species from others in the species level model.

**2.4.2.2. Octocopter UAV hyperspectral and lidar data classification.** We performed two separate species-level classifications using the octocopter UAV data: 1) classification using the hyperspectral data alone, and 2) classification using both hyperspectral and LiDAR data. Both classifications were produced and assessed with the same independent sets of training and validation pixels (Table 4). Thus, the classifications could be directly compared to one another for their accuracies (Foody, 2002; Olofsson et al., 2014). We assessed the user's, producer's, and overall accuracies of each classification using a full confusion matrix with the validation pixels (Table 4) (Congalton and Green, 2002; Foody, 2002).

**Table 3**

Training and validation samples used in the UAV multispectral-photogrammetry fusion for functional cover type classification.

Functional Cover Types	Training sample size (N = 886)	Validation sample size (N = 594)
Shrub	291	143
Herbaceous	202	142
Bare soil	393	309



**Table 4**

Training and validation samples used in the UAV hyperspectral and hyperspectral-LiDAR data classifications. Figs. 1 and 3 show examples and spectral reflectance of these cover types.

ID#	Cover type	Hyperspectral and Hyperspectral-LiDAR CART Training Samples (total N = 695)	Hyperspectral and Hyperspectral-LiDAR CART Validation Samples (total N = 1242)
1	Interspace soil SFMT	173	342
2	Grass soil SFMT	28	149
3	Shrub soil SFMT	241	227
4	Black grama ( <i>Bouteloua eriopoda</i> )	41	120
5	Other grasses (e.g. <i>Muhlenbergia arenicola</i> )	32	53
6	Common forbs (e.g. <i>Asteraceae</i> species)	40	22
7	Four-wing saltbush ( <i>Atriplex canescens</i> )	40	93
8	Creosote bush ( <i>Larrea tridentata</i> )	52	168
9	Ephedra ( <i>Ephedra</i> species)	13	68
10	Shadow	35	–

First, we classified the octocopter UAV hyperspectral image. Using the training samples and all 272 hyperspectral bands (400–1000 nm, Fig. 3) at the corresponding pixel locations, we developed a CART model (Breiman, 1984) in R software (version 3.5.3) using the ‘rpart’ package (Therneau and Atkinson, 2019). In addition to the rationale described above, we chose the CART approach because it offers an efficient method to reduce the 272 spectral bands to a smaller number deemed most important for classification. The binary recursive CART model included 11 spectral bands centered at the following wavelengths distributed across the entire range available among the 272 spectral bands: 402 nm, 408 nm, 428 nm, 502 nm, 506 nm, 513 nm, 531 nm, 546 nm, 660 nm, 725 nm, and 999 nm. We implemented the resulting classification model via the decision tree classifier in ENVI 5.2.

Second, we combined the octocopter UAV hyperspectral data with the corresponding UAV LiDAR data to produce a hyperspectral-LiDAR fusion model. We layer stacked the 7 LiDAR-derived bands with the 272 spectral bands, which resulted in a 279-band image. We developed a predictive CART model using the training samples. Notably, the final hyperspectral-LiDAR classification model included the maximum plant height as an input band along with 10 hyperspectral bands centered at the following wavelengths: 402 nm, 408 nm, 444 nm, 502 nm, 513 nm, 531 nm, 546 nm, 660 nm, 725 nm, and 761 nm. We implemented the final classification tree model in ENVI 5.2 using the decision tree classifier with the input data bands in their native resolution of 6 cm. We additionally implemented the model a second time with the input data resampled to 13 cm resolution via nearest neighbor resampling technique to enable a comparison to the multispectral-photogrammetry fusion species classification at the same spatial resolution.

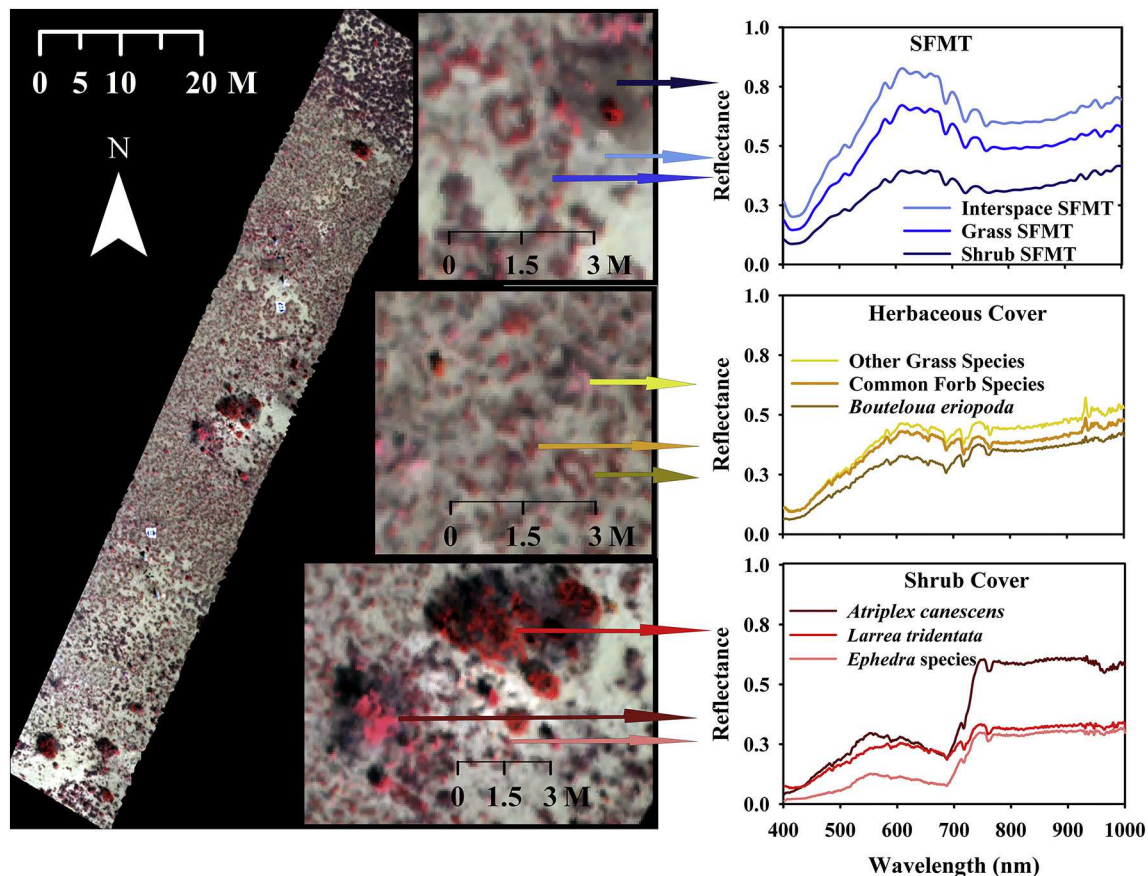


**Fig. 3.** An octocopter UAV hyperspectral image from the prescribed burn rangeland, in which the northeastern edge also illustrates the transition into unburned vegetation for comparison. The hyperspectral image insets illustrate the three studied functional cover types of bare soil, herbaceous plants, and shrubs. We show 3 typical spectra for individual SFMT and plant species. These reflectance data were used as training spectra to produce the hyperspectral image classification outputs shown in Figs. 5 and 6.

## 2.5. Quantifying rangeland soil fertility dynamics

The error of the elevation changes in each ground-based LiDAR DOD was estimated as the sum of squares in quadrature of the georeferencing and registration RMSEs for the z dimension reported in Table 2 for the respective DEMs. For example, this vertical error was estimated for each DOD derived from differencing the 2017 and 2016 DEMs in the burned plots as  $(0.0025^2 + 0.0025^2)^{1/2} = 0.0035$  m. The vertical error similarly estimated for each 2018–2017 DOD in the burned plots was 0.0037 m. The DODs were summarized among the burned plots using the machine learning classification map to determine the mean soil surface elevation change (m) among SFMT and by SFMT, during the first- and second-year post-fire, respectively. Individual pixels in each 2017–2016 DOD exhibiting topographic changes of  $-0.0035$  to  $0.0035$  m were excluded from the summarizations by SFMT as they potentially represented survey registration errors and not actual geomorphic change. Individual pixels in each 2018–2017 DOD exhibiting topographic changes of  $-0.0037$  to  $0.0037$  m were similarly excluded from the summarizations by SFMT.

We quantified nutrient budgets related to post-fire soil erosion and deposition for the burned area using two approaches: first using the functional cover classification derived from the UAV multispectral-photogrammetry fusion, and then using the SFMT classification derived from the hyperspectral-LiDAR fusion. Both approaches also leveraged the ground-based LiDAR change detection results and the soil C and N concentrations measured by Wang et al. (2019a). To estimate the amount of C and N potentially lost or gained due to soil erosion or deposition in the 1 ha burned area during the first and second years post-fire, we used eqs. 1 and 2, respectively.

$$C_{kg} = C_{fraction} * A_{bs} * D * bd \quad (1)$$

$$N_{kg} = N_{fraction} * A_{bs} * D * bd \quad (2)$$

$C_{kg}$  and  $N_{kg}$  are the mass (kg) of C and N potentially lost or gained.  $C_{fraction}$  and  $N_{fraction}$  are the soil fractional C and N contents (Wang et al., 2019a).  $A_{bs}$  is the total area ( $m^2$ ) covered by the single class “bare soil” (i.e., not differentiated by SFMT) determined within the fixed-wing UAV multispectral-photogrammetry functional cover classification.  $D$  is the depth (m) of soil erosion or deposition determined with ground-based LiDAR, and  $bd$  is soil bulk density of  $1500 \text{ kg/m}^3$ .

To estimate the amount of C and N potentially lost or gained on the three different SFMT, we used eqs. 3 and 4, respectively.

$$C_{sfmt\_kg} = C_{sfmt\_fraction} * A_{sfmt} * D_{sfmt} * bd \quad (3)$$

$$N_{sfmt\_kg} = N_{sfmt\_fraction} * A_{sfmt} * D_{sfmt} * bd \quad (4)$$

$C_{sfmt\_kg}$  and  $N_{sfmt\_kg}$  are the mass (kg) of C and N potentially lost or gained by SFMT.  $C_{sfmt\_fraction}$  and  $N_{sfmt\_fraction}$  are the SFMT fractional C and N contents (Wang et al., 2019a).  $A_{sfmt}$  is the area ( $m^2$ ) covered by each SFMT determined with the octocopter UAV hyperspectral-LiDAR classification.  $D_{sfmt}$  is the depth (m) of soil erosion or deposition determined by SFMT with ground-based LiDAR.

## 3. Results

### 3.1. UAV multispectral-photogrammetry fusion classification

The classification of the fixed-wing UAV multispectral-photogrammetry fusion imagery had an overall accuracy of 95% in separating the three functional cover types of shrub, herbaceous, and bare soil cover (Table 5; Fig. 4). Among the three classes, bare soil cover had the highest producer's accuracy of 96% with a user's accuracy of 95%. Shrub cover type had a producer's accuracy of 93% and user's accuracy of 96%, while herbaceous cover type had 94% and 96% producer's and user's accuracies, respectively. Despite these accuracies,

**Table 5**

Accuracies and mapped area in the UAV multispectral-photogrammetry fusion for functional cover type classification.

Functional Cover Types	Producer's Accuracy (%)	User's Accuracy (%)	Cover (%) in Burned Rangeland (0.7 ha)	Cover (%) in Unburned Rangeland (3.45 ha)
Shrub	93	96	7	23
Herbaceous	94	96	15	30
Bare soil	96	95	78	47
Overall Accuracy = 95%				

herbaceous cover type in small patches appears underclassified (Fig. 4) and often combined into bare soil likely due to the low reflectance in the NIR band. Of the entire 4.15 ha of burned and unburned rangeland that were classified in the fixed-wing UAV image extent, 0.85 ha or 20% were classified as shrub cover type, 28% as herbaceous cover type, and 52% as bare soil. Within the 0.7 ha portion of the data that was burned rangeland, 7% were classified as shrub cover type, whereas the adjacent unburned rangeland had 23% of the area classified as shrub cover type. The burned portion of the study area had 78% bare soil compared to the unburned area, which had 47% of its total area classified as bare soil. Within the burned portion of the classified study area, herbaceous cover comprised 15%, compared to 30% in the unburned rangeland. Thus, the unburned rangeland had 3-times greater shrub cover area compared to the burned rangeland. Conversely, the burned rangeland included much greater bare soil cover compared to the unburned rangeland indicating many of the small, carbon- and nutrient-rich, shrub and grass SFMT that developed beneath the former plant canopies had become exposed to soil erosion processes.

The fixed-wing UAV multispectral-photogrammetry image with 6 bands did not produce an accurate classification model for the 9 plant species and SFMT; the overall accuracy was only 36%. All producer's accuracies were lower than 68%, which was observed for the interspace SFMT class, but with a user's accuracy of 40%. As a result, the fixed-wing UAV multispectral-photogrammetry image classification output was not used for further comparison between burned and unburned rangelands or area estimates for the 9 different plant species and SFMT, and the octocopter UAV hyperspectral-LiDAR methods were pursued for those purposes instead (below).

### 3.2. UAV hyperspectral image classification

Classification of the octocopter UAV hyperspectral image excluding LiDAR produced an overall accuracy of 71% for the 9 rangeland plant species and SFMT (Table 6). Among the 9 classes, interspace SFMT had the highest producer's accuracy of 95% with a user's accuracy of 90% likely due to its high reflectance across most of the spectral bands. Shrub SFMT class had 67% producer's accuracy, whereas grass SFMT was largely misclassified as shrub SFMT. One particularly advantageous result from the hyperspectral image classification was that none of the SFMT types were misclassified as the overlying cover of any of the plant species. Creosote bush had a 100% producer's accuracy and 93% user's accuracy (Table 6). Despite their low abundance, both ephedra and four-wing saltbush were well classified with 85% and 78% producer's accuracies and 73% and 100% user's accuracies, respectively (Table 6). Black grama also had a high producer's accuracy of 83% in the hyperspectral image classification with a user's accuracy of 71% (Table 6). However, common forbs and other grass species were rarely detected, likely due to their very low abundance.

The hyperspectral image classification indicated widespread unvegetated, bare soil cover across both the burned and unburned rangelands. Specifically, SFMT cover types collectively covered 89% of the burned area. Among them, the shrub SFMT was dominant, covering 61% of the total burned area. Interspace SFMT was the second most common cover type and comprised 28% of the burned study area. In comparison,



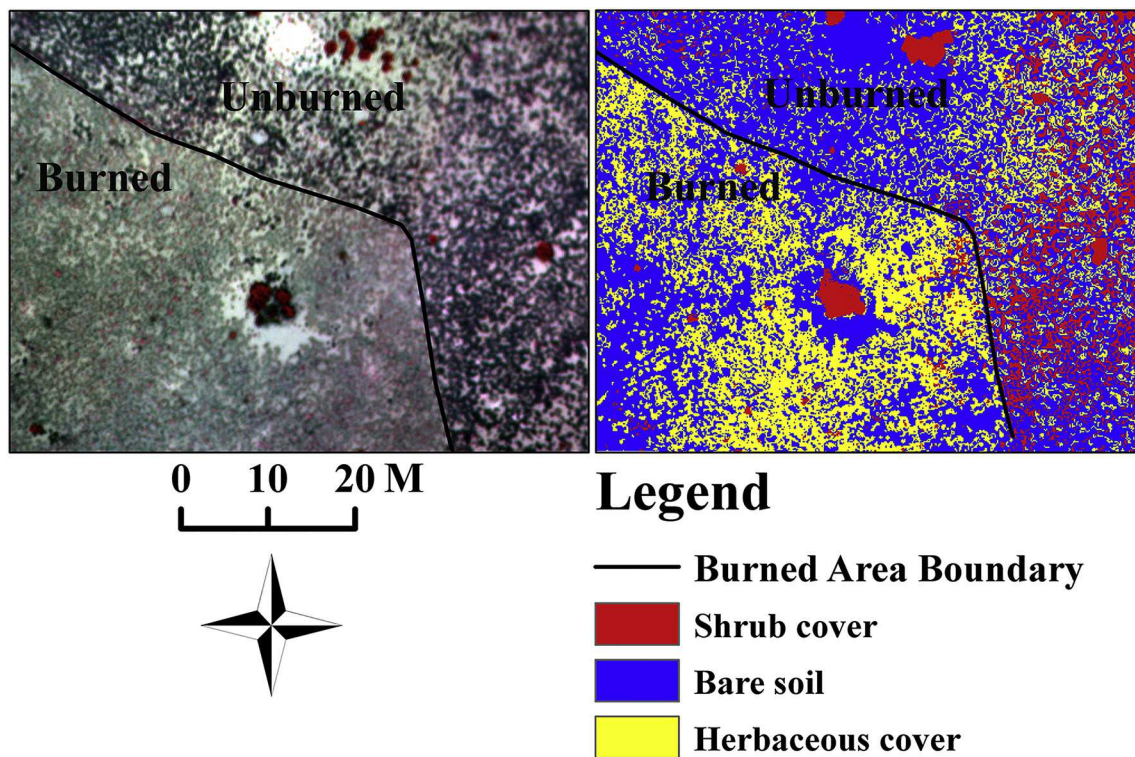


**Fig. 4.** A fixed-wing UAV multispectral image with 13-cm spatial resolution, displayed in false color composite (left panel), and resulting classification (right panel) of the primary rangeland functional cover types: shrub cover, herbaceous cover, and bare soil. The multispectral image example is from an area along the boundary of burned and unburned rangelands. In both rangelands, small patches of plants and bare soil are clearly visible and can be classified by functional cover type to make inferences about the primary plant cover and SFMT, where distinct spatial patterns of soil nutrients and carbon occur in the unburned rangeland and are altered due to fire disturbance in the burned rangeland.

**Table 6**

Accuracies using the UAV hyperspectral data alone and the UAV hyperspectral-LiDAR fusion to classify plant species and SFMT at 6 cm resolution. “Common forbs” and “Other grasses” with low accuracies covered <1% of the rangeland. “Shadow” class is not assessed.

ID#	Cover Type	Hyperspectral Producer's accuracy (%)	Hyper-spectral User's accuracy (%)	Hyperspectral-LiDAR fusion Producer's accuracy (%)	Hyperspectral-LiDAR fusion User's accuracy (%)	Overall accuracy
1	Interspace soil SFMT	95	90	93	97	
2	Grass soil SFMT	0	0	93	83	
3	Shrub soil SFMT	67	41	73	95	
4	Black grama ( <i>Bouteloua eriopoda</i> )	83	71	94	66	
5	Other grasses (e.g. <i>Muhlenbergia arenicola</i> )	9	16	81	49	
6	Common forbs (e.g. <i>Asteraceae</i> species)	0	0	72	100	
7	Four-wing saltbush ( <i>Atriplex canescens</i> )	78	100	77	100	
8	Creosote bush ( <i>Larrea tridentata</i> )	100	93	98	98	
9	Ephedra ( <i>Ephedra</i> species)	85	73	81	96	
10	Shadow	–	–	–	–	
Hyperspectral						71%
Hyperspectral-LiDAR fusion						87%

total bare soil cover at the unburned rangeland was lower, where shrub SFMT comprised 44% of the total area. Another important difference observed between the burned and unburned rangelands was the distribution of black grama grass: it comprised nearly three times greater cover in the unburned rangeland compared to the burned rangeland. In addition, ephedra and four-wing saltbush, which were relatively well classified compared to creosote bush, covered only 1% of the burned rangeland, but collectively covered 7% of the entire unburned rangeland.

### 3.3. UAV hyperspectral-LiDAR fusion classification

Classification of the hyperspectral-LiDAR fusion image produced an overall accuracy of 87% for the 9 plant species and SFMT (Table 6). Among the 9 classes (Fig. 5), creosote bush had the highest producer's accuracy of 98% with a similarly high user's accuracy of 98% (Table 6). Interspace SFMT had a high producer's accuracy of 93% and a user's accuracy of 97% (Table 6). Black grama grass also had a high producer's accuracy of 94%, but a lower user's accuracy of 66% (Table 6). Among the 9 classes, shrub SFMT were sometimes confused with black grama



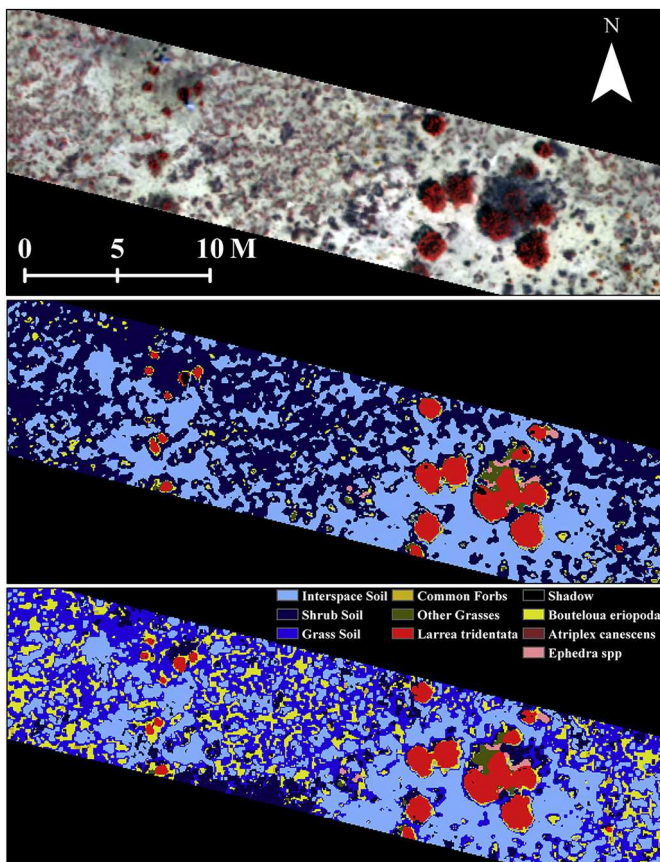


**Fig. 5.** An octocopter UAV hyperspectral image from the burned rangeland displayed in false-color composite using 3 spectral bands (top panel) and a resulting plant species and soil fertility microsite types (SFMT) classification (71% overall accuracy; middle panel). The same hyperspectral image is fused with the octocopter UAV LiDAR data to similarly produce a plant species and SFMT classification shown in the bottom panel that is more accurate (87% overall accuracy, bottom panel). In the fusion-based approach, small differences in plant heights are leveraged to further separate functional cover types into refined patches of plant species and SFMT.

grass, likely due to their similar spectra in the green and near-infrared bands (Fig. 3) and similar height above the neighboring interspace SFMT. This resulted in producer's accuracy of 73% for the shrub SFMT, but a high user's accuracy of 95%, which is much greater than its user's accuracy in the hyperspectral image classification (Table 6). Similar to the hyperspectral image classification, the ephedra and four-wing salt-bush both had high producer's accuracies of 81% and 77%, respectively, with 96% and 100% user's accuracies (Table 6). Compared to the hyperspectral image alone, the hyperspectral-LiDAR fusion substantially increased the detection accuracies for common forbs (72% producer's accuracy), which was often confused with shrub SFMT in the hyperspectral image classification. Producer's accuracy for other grass species improved from 9% to 81% with the fusion classification, whereas black grama producer's accuracy increased from 83% to 94%. Another large improvement was observed for grass SFMT, which increased from no detection in the hyperspectral data to 93% producer's accuracy with 83% user's accuracy in the fusion-based classification (Table 6).

The hyperspectral-LiDAR fusion classification indicated that the overall distribution of total vegetation and SFMT cover types were similar between the burned versus the unburned portions of the study area. However, the detailed species classification revealed several unique patterns: a) the burned area included only 4% creosote bush cover, whereas the unburned area had more than twice as much creosote bush at 11% cover, b) although the total herbaceous cover was similar

between burned and unburned rangelands, black grama covered only 2% of the burned area, whereas its cover was three times greater and covered 6% of the unburned rangeland, and c) the common forb cover at the burned rangeland was twice as high compared to the unburned, although its total cover was low at 1.2%. Interestingly, overall bare soil cover (i.e., of all SFMT types combined) was similar (79%) between the burned and unburned rangelands. We expected that the area classified as shrub SFMT might be much higher in the burned area owing to the removal of the overlying shrub (e.g., creosote) plant canopies by fire six months prior, but it was lower at 19% at the burned compared to 24% at the unburned rangelands; this unexpected result might be in part influenced by the confusion between shrub SFMT and black grama grass.

When we implemented the UAV hyperspectral-LiDAR fusion classification with the input data resampled to 13 cm, the overall accuracy decreased to 66%, which was nearly two times more accurate than the species classification based on the fixed-wing multispectral-photo-grammetry fusion in the same spatial resolution. Thus, the UAV hyperspectral-LiDAR fusion clearly produced the best of the tested approaches for mapping the spatial distribution of plant species and SFMT at the very fine ( $10^{-3}$ – $10^{-1}$  m) scale of individual plant canopies and inter-canopy areas in rangelands (Fig. 6). However, the spatial resolution of the UAV-based LiDAR survey data is considerably lower compared to the survey-grade ground-based LiDAR instrument (Fig. 6), and thus the latter was investigated (below) to accurately measure the source and sink dynamics for sediment and adsorbed nutrients when SFMT are exposed to enhanced erosion following disturbance by fire.

#### 3.4. Ground-based LiDAR: Image classification and topographic change detection

The ground-based lidar data, photos, and machine learning classification of the photos (Fig. 7A, B) highlight in the burned rangeland that the prescribed fire removed most of the aboveground biomass from each SFMT. Immediately after the fire, light-colored ash, dark-colored ash, and mineral soil remained on the SFMT previously covered by shrub vegetation, grass (herbaceous) vegetation, and bare soil (i.e., interspace), respectively (Fig. 7A). One-year post-fire, the plots had eroded on average (Table 7); grasses had reemerged on the plots not only in the SFMT previously covered by grass and herbs, but also in some SFMT previously covered by shrub vegetation or interspace soil (Fig. 7A, B). Small-statured shrubs had also resprouted in some but not all the shrub SFMT (Fig. 7A, B). Two-years post-fire, all plots had aggraded very slightly, though not significantly, from sediment deposition on average (Table 7); canopies of resprouted shrubs had grown larger, though the overall spatial pattern of the three SFMT types was fairly similar to the beginning of the study (Fig. 7A, B).

Fig. 7C shows an example from the same burned monitoring plot depicted in Fig. 7A and B and illustrates that a shift in spatial patterns of soil erosion and deposition occurred during the two years post-fire. Fig. 7D and Table 7 quantify the results by SFMT for all burned plots. Soil erosion was more spatially widespread during the first-year post-fire (Fig. 7C); shrub, grass, and interspace SFMT eroded on all plots on average (Fig. 7D; Table 7). During the second-year post-fire, the area of soil deposition was more comparable in area to erosion and both occurred in small patches (Fig. 7C); shrub SFMT eroded on average, whereas grass and interspace SFMT aggraded due to soil deposition (Fig. 7D, Table 7). Thus, all three SFMT types clearly functioned as sediment sources for soil erosion in year 1, but then the grass and interspace SFMT shifted to function as sinks for soil deposition in year 2, post-fire. In comparison, on the control plots that were not burned, the bare soil surfaces of the interspace SFMT eroded on average during years 1 and 2 (mean elevation changes = 0.009 and 0.002 m, respectively), though not significantly in year 2 (standard error of elevation changes = 0.0007 and 0.0058 m, respectively).

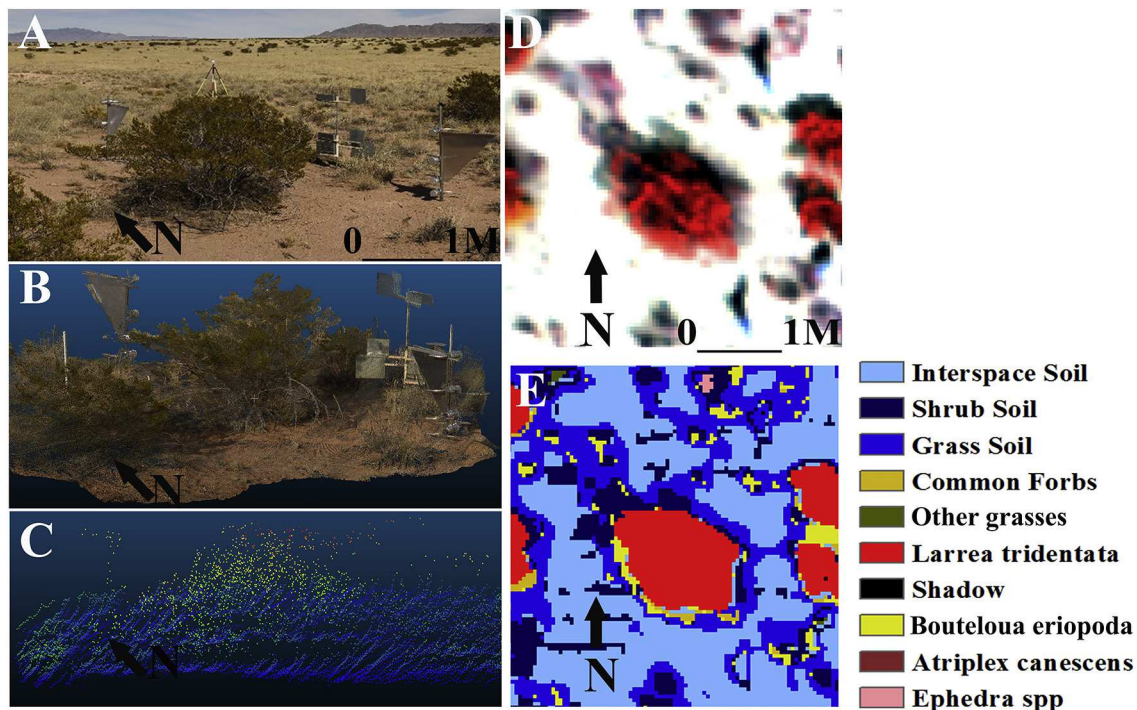


**Fig. 6.** A study plot example within the unburned rangeland that was classified by plant species and soil fertility microsite types (SFMT) using the octocopter UAV platform with hyperspectral and LiDAR sensors, and which was also scanned with the Riegl VZ-1000 ground-based LiDAR instrument. The example of unburned control plot is shown in panel A. The very high density, colored, ground-based LiDAR point cloud is depicted in panel B for comparison with the LiDAR point cloud acquired from the sensor onboard the UAV platform (panel C). The hyperspectral image of the plot is displayed in false-color composite using 3 spectral bands (panel D) for comparison with the plant and SFMT classification derived from the UAV-based hyperspectral-LiDAR fusion (panel E).

### 3.5. Rangeland soil fertility dynamics

#### 3.5.1. Fertility dynamics by bare soil functional cover

Wang et al. (2019a) measured soil C and N contents of 1.04% and 0.08% (means of  $N = 150$  samples) respectively, in the burned rangeland near the time of our UAV image acquisitions. The fixed-wing multispectral-photogrammetry classification indicated that 78% of the burned rangeland was bare soil of all three burned, unvegetated SFMT types combined, and thus susceptible to erosion after the fire. The ground-based LiDAR surveys indicated that the burned study plots eroded an average of  $-0.0121$  m in the first year after the prescribed fire, whereas they aggraded by an average of  $0.0001$  m in the second year after the prescribed fire (Table 7). Extrapolating these observations to the entire 1 ha, we estimate that the burned rangeland potentially lost C and N to soil erosion during the first year, but potentially gained C and N from soil deposition during the second year, after the prescribed fire (Table 8).

#### 3.5.2. Fertility dynamics by SFMT

The ground-based LiDAR results indicated that the shrub SFMT eroded during the first and second year post-fire, whereas the grass and interspace SFMT eroded during the first year but aggraded during the second year. The UAV hyperspectral-LiDAR classification indicated that the burned rangeland in the image was comprised of: 19% shrub SFMT; 38% grass SFMT, and 23% interspace SFMT. Wang et al. (2019a) measured SFMT C and N contents (means of approximately 50 samples per SFMT type from the dataset of 150 total samples described in subsection 3.5.1) in the burned rangeland near the time of our UAV image acquisitions: 1.51% C and 0.12% N in the shrub SFMT; 1.09% C and 0.08% N in the grass SFMT, and 0.95% C and 0.07% N in the interspace SFMT. Combining the UAV hyperspectral-LiDAR classification, elevation change results from the ground-based LiDAR, and Wang et al. (2019a) results, we estimate that the shrub SFMT within the burned

rangeland potentially lost C and N due to soil erosion during the first and second years after the prescribed fire (Table 9). We estimate the grass and interspace SFMT also lost C and N due to soil erosion during the first year after the prescribed fire (Table 9). However, the grass and interspace SFMT aggraded during the second year post-fire, and we infer that the source of the sediment was the shrub SFMT which eroded during both years; this inference is also supported by the results of Dukes et al. (2018), Gonzales et al. (2018), Ravi et al. (2019), and Wang et al. (2019a, 2019b). Thus, we use soil C and N contents for the shrub SFMT type (i.e., 1.51% C and 0.12% N, Wang et al., 2019a) to estimate that during the second year post-fire grass and interspace SFMT potentially gained C and N (Table 9).

## 4. Discussion

### 4.1. Mapping rangeland plant species and soils with UAV data fusion

High spatial and spectral resolution remote sensing data are required to track many of the key dynamics and feedbacks that shape rangeland ecosystems. While the fixed-wing UAV multispectral-photogrammetry fusion image can be used to classify rangeland plant functional groups (Fig. 4), both the spatial and spectral resolution of these data limit their utility in classifying rangeland plants at the species level. This is likely because several species are similar in height and spectral reflectance across the limited number of bands in the photogrammetry data; these spectral similarities can be observed in the hyperspectral spectra in Fig. 3. For example, black grama grass and its mix with other species and SFMT might have made the species classification challenging.

The classification of rangeland functional cover types using the UAV multispectral-photogrammetry image does offer two important utilities. First, the 13 cm pixels resolve very small patches of individual shrubs, herbaceous plants, and bare soil (Fig. 4), although these are aggregated functional cover types only. Secondly, the functional cover type map is

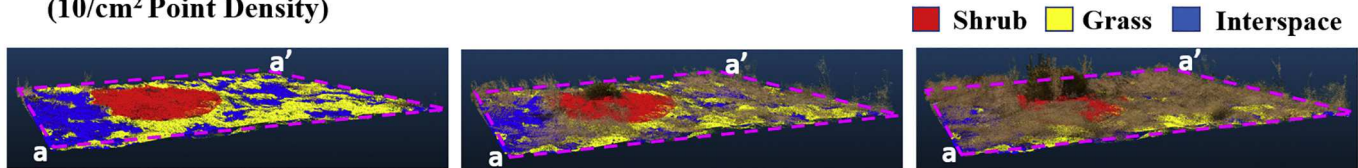


## A. Ground-based LiDAR Survey Images Used in Machine Learning Classification of SFMT

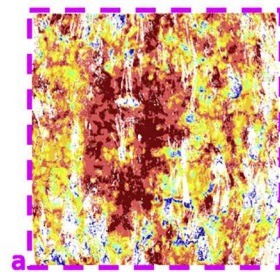
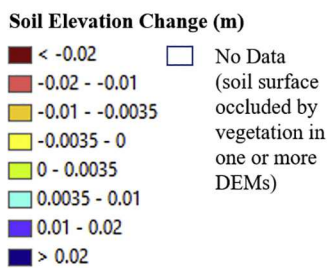
Study plot dimensions = 5 x 5 m



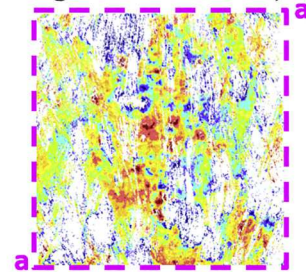
## B. Classification of SFMT and Bare Earth & Vegetation Point Clouds (10/cm<sup>2</sup> Point Density)



## C. 1-cm Resolution Bare Earth DEMs of Difference (DoD) (georeferencing RMSE <0.01cm)



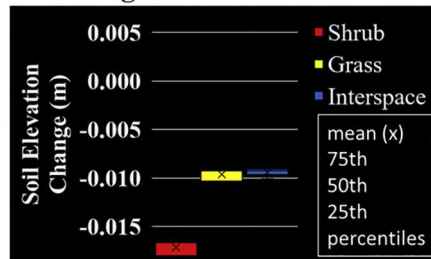
1 week to  
1 year post-fire



1 to 2 years  
post-fire

## D. Sources and Sinks of Rangeland Sediment & Nutrients Quantified from 2 DoDs over 3 years

All SFMT erode and function as sources of sediment and adsorbed nutrients for the surrounding environment during year 1 post-fire



Grass and interspace SFMT function as sediment and nutrient sinks during year 2 post-fire



**Fig. 7.** Results obtained from using ground-based LiDAR to monitor rangeland soil fertility microsite types (SFMT) to characterize the source and sink dynamics of sediment and adsorbed nutrients at very high resolution and spatial accuracy. (A.) Example of mosaicked digital images acquired from the calibrated LiDAR-mounted camera during the LiDAR scans for one of the study plots in 2016, 2017, and 2018. (B.) Bare earth LiDAR point cloud colored by the machine learning SFMT classification and overlain by the vegetation points in each respective LiDAR point cloud for the example study plot. (C.) DODs derived from change detection of bare earth DEMs for 2016–2017 & 2017–2018 time series, respectively, from the example study plot. In the DODs, cool colors show locations of soil and adsorbed nutrient deposition and warm colors show locations of erosion caused by sediment transport associated with the disturbance of rangeland vegetation by fire and subsequent recovery of vegetation. Note that the same study plot is depicted in A, B and C but the vantage point differs (e.g., see the location of plot corners marked a and a' in each panel.). (D.) Soil surface elevation change (m) caused by erosion or deposition of soil determined from the DODs for the first- and second-year post-fire for all the burned monitoring plots. Note the shift in source and sink dynamics for sediment and adsorbed nutrients with post-fire recovery of the rangeland.

**Table 7**

Elevation changes determined from the DODs among the three plots in the burned rangeland owing to soil erosion (–) or deposition (+), respectively, during the first- and second-years post-fire. Changes are summarized among SFMT (i.e., “Total”) and by SFMT.

Year	Total		Shrub Soil SFMT		Grass Soil SFMT		Interspace Soil SFMT	
	Mean (m)	SE (m)	Mean (m)	SE (m)	Mean (m)	SE (m)	Mean (m)	SE (m)
1	–0.0121	0.0013	–0.0172	0.0009	–0.0097	0.0007	–0.0094	0.0003
2	0.0001	0.0013	–0.0026	0.0008	0.0006	0.0025	0.0023	0.0029

useful to make inferences about disturbance impacts on the spatial distribution of rangeland nutrients and C storage at the soil surface. For example, by comparing the burned and unburned rangelands, we estimate 70% reduction in shrub cover six months after the prescribed fire, which in turn makes the small patches of nutrients and C that previously accumulated at the soil surface beneath the shrubs more susceptible to erosion processes. This type of information, especially when combined

with the photogrammetry-derived plant height estimates, has a good potential for monitoring shrub-encroached rangelands (Cunliffe et al., 2016a; Sankey et al., 2019). In the western US, woody species such as creosote bush, mesquite, and pinyon-juniper are encroaching across >10 Mha of desert grassland with relative cover increases of up to 600% in some cases, owing to drought, changing climate, and land use policies (Munson et al., 2013; Peters et al., 2012; Romme et al., 2009; Sankey



**Table 8**

Estimated soil, soil C, and soil N lost (–) or gained (+) by the burned rangeland owing to soil erosion or deposition, respectively, during the first- and second-years post-fire.

Year	Soil (kg/ha)	C (kg/ha)	N (kg/ha)
1	–141,298	–1474	–113
2	1339	14	1

et al., 2013). Land managers interested in monitoring shrub encroachment at a local scale can use UAV multispectral images and associated 3D data to guide management decisions such as burning or thinning treatments (Sankey et al., 2019).

Species-level classification and rangeland monitoring require UAV hyperspectral imagery (Fig. 5), which offers a unique capability to detect and estimate the cover and abundance of specific species of interest. For example, black grama is a native grass species in many grasslands of the southwestern USA and is an important indicator species of a healthy, stable rangeland (Munson et al., 2013). Land managers actively monitor and develop management prescriptions for this species in the region (Munson et al., 2013). Similarly, creosote bush is a common native shrub species across many southwestern USA rangelands (Grover and Musick, 1990; Munson et al., 2013, 2016), and a driver of shrub encroachment in grasslands, that can be identified with a high user's accuracy. Land managers interested in monitoring those species at the level of individual plants can benefit from UAV hyperspectral images similar to manned airborne hyperspectral data (Asner and Heidebrecht, 2002). Furthermore, the UAV hyperspectral image can be used to identify soil types that differ by levels of C storage and nutrient accumulation at the surface. Six months after the prescribed fire at our burned rangeland, for example, up to 89% of the land surface consisted of the combination of the three SFMT without any overlying plant canopy cover. Published laboratory-based measurements indicate significant differences in soil nutrient and C accumulation among the three different SFMT that we mapped with the hyperspectral image (Wang et al., 2019a, 2019b).

Our second objective involved evaluating how hyperspectral-LiDAR fusion outperforms hyperspectral data alone in this application. As expected, the fusion approach resulted in greater overall accuracy, greater separation between the soil surfaces (SFMT) versus vegetation species, and better detection of individual species. Sankey et al. (2017b) found that fusion of UAV LiDAR with hyperspectral imagery increased overall classification accuracy by approximately 12% over hyperspectral data alone when classifying rangeland plant species. Here, using a similar approach but also incorporating classification of soil surface types, our gain in overall accuracy was similar but slightly more pronounced at 16%. The improvements likely resulted from the small differences in plant height associated with the vegetation patches around which these soil surface types and associated C, N, and other nutrients accumulate (Dukes et al., 2018; Wang et al., 2019a, 2019b). Using the hyperspectral image alone, the shrub SFMT were commonly confused with black grama and sometimes with ephedra, both of which have relatively low reflectance compared to other green vegetation across the red, red edge, near infrared, and other spectral regions (Fig. 3). UAV hyperspectral-LiDAR fusion improved our ability to separate these classes.

**Table 9**

Estimated soil, soil C, and soil N lost (–) or gained (+) by SFMT within the burned rangeland owing to soil erosion or deposition, respectively, during the first- and second-years post-fire.

Year	Shrub Soil SFMT			Grass Soil SFMT			Interspace Soil SFMT		
	Soil kg/ha	C kg/ha	N kg/ha	Soil kg/ha	C kg/ha	N kg/ha	Soil kg/ha	C kg/ha	N kg/ha
1	–48,881	–739	–59	–55,032	–602	–46	–32,514	–308	–23
2	–7386	–112	–9	3548	54	4	7978	121	10

#### 4.2. Quantifying soil surface fertility with ground-based LiDAR, UAV, and data synthesis

The fixed-wing UAV multispectral-photogrammetry classification indicated that vegetation cover was, as expected, lower on the burned compared to unburned rangeland six months after the prescribed fire. Soil that lacks a protective cover of vegetation is vulnerable to erosion in rangelands (Breshears et al., 2003; Lee, 1991a, 1991b; Okin and Gillette, 2001; Okin, 2008). The burned study plots eroded in the first year after the prescribed fire, but aggraded slightly due to soil deposition in the second year post-fire, during which the burned area is estimated to have become a net nutrient sink for 14 kg/ha of C and 1 kg/ha of N. These analyses quantify the nutrient source and sink dynamics over time for the burned area as a whole, although they obviously don't elucidate dynamics between the SFMT within the burned rangeland.

A strength of the UAV hyperspectral-LiDAR fusion is that it permitted the accurate classification of vegetation by species as well as bare, unvegetated soil by SFMT. The shrub SFMT eroded during years 1 and 2 after the prescribed fire, whereas the grass and interspace SFMT eroded during year 1 but aggraded during year 2. Thus, in contrast to the shrub SFMT, the grass and interspace SFMT shifted from functioning as net sources to net sinks for sediment and adsorbed nutrients during the second-year post-fire. The total nutrient sink due to soil deposition on grass and interspace SFMT during the second year post-fire was approximately 1.5 times greater than the C and N lost from erosion on the shrub SFMT during the second year after the fire, and equivalent to approximately 1/5 of the C and N lost from shrub SFMT during the entire two-year experiment (Table 9). These C and N source and sink estimates are scaled to the entire 1 ha burned rangeland in our study. In a global context, prescribed and wildfires burn an estimated 423 Mha every year (Giglio et al., 2018) largely in desert grasslands of all continents especially Africa, Australia, and Central Asia (Abreu et al., 2017; Andela et al., 2019; Scholes and Archer, 1997). Post-fire erosion can potentially degrade rangelands (Sankey et al., 2009; Sankey et al., 2012b). However, in shrub-encroached rangelands, fire might also help redistribute soil nutrients in spatial patterns that concentrate the resources near grasses providing them a competitive advantage relative to shrubs (Dukes et al., 2018; Gonzales et al., 2018; Wang et al., 2019a, 2019b). Spatially explicit quantification of these processes and management effects was achieved in our study owing to the very high spatial and spectral resolution UAV data.

#### 4.3. Current limitations and future research

It can be challenging to accurately classify species that cover a small portion of the total landscape. The “common forb” and “other grasses”, which were classes that comprised a small portion of the landscape, were not detected or well classified (Table 6), although the shrub species of ephedra and four-wing saltbush were well classified in the UAV hyperspectral image despite their combined low abundance. Detecting rare cover types often leads to high omission errors and subsequent overestimation of the areas covered by the target species, as well as underestimation of other more abundant cover types (Elkind et al., 2019; Sankey et al., 2014). Further testing and detection methods development are still necessary for the small herbaceous species at low abundance, even with the high spectral and spatial resolution UAV

hyperspectral data. One possible improvement that needs to be tested is the intentionally disproportionate increase in the field-based training samples for the rare species. Our study includes a relatively proportionate distribution of field-based training samples, where rare species are represented by fewer samples, whereas the dominant species are represented by more samples. In contrast, previous studies with coarse resolution satellite images disproportionately oversampled the rare cover types to improve detection accuracies of such classes (Congalton and Green, 2002; Massey et al., 2018; Sankey et al., 2018). Such a strategy would require greater numbers of field-based samples (Foody, 2002; Olofsson et al., 2014), which would also require much greater image extent covered by the UAV platform.

Another consideration for future work is to leverage the strengths of UAV hyperspectral data to complement satellite-based remote sensing of rangelands. Our UAV hyperspectral image classification included 11 spectral bands that overlap with spectral ranges available in some satellite sensors including WorldView-2, WorldView-3, and Sentinel-2. The 11 bands used in the model span the entire spectral range of the 272 total available bands. However, the UAV hyperspectral bands are also very narrow, and thus the set of 11 bands included four specific wavelengths in the blue region (402 nm, 408 nm, 428 nm, and 502 nm) and another four in the green spectral region (506 nm, 513 nm, 531 nm, and 546 nm). Although satellite sensors similarly include the blue and green spectral regions, each of these regions are covered by a single wide spectral band in satellite data and, therefore, cannot leverage the nuanced reflectance changes from one band to another within each region. The many narrow spectral bands in the hyperspectral data provide unique opportunities to detect individual plant species and SFMT, while spanning similar overall spectral range as satellite images. The fine spatial resolution in the UAV hyperspectral data was similarly critical in detecting the small vegetation and bare soil patches common in rangelands, which are not detectable in coarser resolution satellite images with <10 m pixels.

Finally, we highlight several strengths of UAV hyperspectral-LiDAR fusion for imaging short, small, sparse plant canopies, which we believe warrant further evaluation in rangelands. Notably, detection of the less common forb and grass species in the hyperspectral-LiDAR fusion was substantially higher, but the low density of those species might have resulted in reflectance values that were mixed with the underlying soil surface throughout the hyperspectral data spectrum (Fig. 3). When combined with the plant height information, the small patches were effectively detected. The fusion of hyperspectral data with LiDAR data also increased producer's accuracies for common shrub species. Mapping woody rangeland plants is important for accurate estimates of the increased C storage, decreases in evapotranspiration and albedo, and increases in runoff, which are projected to occur in the future based on current estimates of shrub encroachment rates, and are projected to provide feedbacks to the regional climate (Browning et al., 2008; Huenneke et al., 2002; Knapp et al., 2008; Scholes and Archer, 1997).

## 5. Conclusions

UAV multispectral-photogrammetry fusion can accurately map plant and soil functional cover types, whereas UAV hyperspectral-LiDAR fusion can accurately detect plant species and SFMT in rangelands degraded by shrub encroachment and disturbed by fire. Synthesis of UAV datasets with ground-based LiDAR surveys and laboratory characterization of soils quantitatively explains how prescribed fire in a shrub-encroached grassland can be used to alter the spatial patterning of nutrients at the soil surface and thus counter ecosystem effects of encroachment that degrade grassland habitat. Plant-soil-nutrient dynamics in rangelands and other ecosystems with small patches of low stature vegetation can be monitored at fine spatial scales via these UAV and ground-based LiDAR remote sensing data fusion approaches. The UAV and ground-based LiDAR data cover small spatial extents that are

relevant to rangeland managers, and they provide detailed information that can be leveraged in more accurate accounting of C and nutrient fluxes that commonly occur at the soil surface in rangeland ecosystems.

## Credit author statement

**Joel B. Sankey:** Conceptualization, Methodology, Formal Analysis, Investigation, Writing – Original Draft, Writing – Review & Editing, Funding Acquisition, Project Administration. **Temuulen T. Sankey:** Conceptualization, Methodology, Formal Analysis, Investigation, Writing – Original Draft, Writing – Review & Editing, Funding Acquisition, Project Administration. **Junran Li:** Conceptualization, Writing – Review & Editing, Funding Acquisition, Project Administration. **Sujith Ravi:** Conceptualization, Writing – Review & Editing, Funding Acquisition, Project Administration. **Guan Wang:** Investigation. **Alan Kasprak:** Investigation, Writing- Reviewing and Editing, Methodology. **Joshua Caster:** Investigation, Methodology.

## Declaration of Competing Interest

The authors declare that they have no known competing financial interests or personal relationships that could have appeared to influence the work reported in this paper.

## Acknowledgements

This research was funded by the US National Science Foundation (NSF) EAR-1451518 for S. Ravi and EAR-1451489 for J. Li. The authors gratefully acknowledge the contributions of Jon Erz and Andy Lopez (FWS, SNWR), and Scott Collins (Sevilleta LTER, New Mexico, USA) for providing access to field and laboratory facilities and technical guidance. The UAV remote sensing equipment purchased for this study was funded by the Office of the Vice President for Research at Northern Arizona University. Joel Sankey was additionally supported by the U.S. Geological Survey Ecosystems Mission Area. The authors acknowledge Keith Kohl of the U.S. Geological Survey for helpful assistance with RTK-GPS survey logistics and analysis. The authors acknowledge RSE Editor-in-Chief Marie Weiss, three anonymous reviewers, and Seth Munson (USGS) for their helpful comments on previous versions of the manuscript. This manuscript is submitted for publication with the understanding that the US Government is authorized to reproduce and distribute reprints for Governmental purposes. Any use of trade, product or firm names is for descriptive purposes only and does not imply endorsement by the US Government.

## Appendix A. Supplementary data

Supplementary data to this article can be found online at <https://doi.org/10.1016/j.rse.2020.112223>.

## References

- Briske, D.D., 2017. Rangeland Systems: Processes, Management and Challenges. Springer.
- Abreu, R.C.R., Hoffmann, W.A., Vasconcelos, H.L., Pilon, N.A., Rossatto, D.R., Durigan, G., 2017. The biodiversity cost of carbon sequestration in tropical savanna. *Sci. Adv.* 3 (e1701284), 2017. <https://doi.org/10.1126/sciadv.1701284>.
- Allred, K.W., 1996. Vegetative changes in New Mexico rangelands. *N. M. J. Sci.* 36, 168–231.
- Andela, N., Morton, D.C., Giglio, L., Paugam, R., Chen, Y., Hantson, S., Werf, G.R., Randerson, J.T., 2019. The global fire atlas of individual fire size, duration, speed and direction. *Earth Syst. Sci. Data* 11 (2), 529–552.
- Angelopoulou, T., Tziolas, N., Balafoutis, A., Zalidis, G., Bochtis, D., 2019. Remote sensing techniques for soil organic carbon estimation: a review. *Remote Sens.* 11, 676.
- Archer, S.R., 1996. Assessing and interpreting grass-woody plant dynamics. In: Hodgson, J., Illius, A.W. (Eds.), *The Ecology and Management of Grazing Systems*. CAB International, Wallingford, UK, pp. 101–134.
- Archer, S.R., Andersen, E.M., Predick, K.I., Schwinning, S., Steidi, R.J., Woods, S.R., 2017. Woody Plant encroachment: Causes and consequences. In: Briske, D.D. (Ed.),

2017. *Rangeland Systems: Processes, Management and Challenges*. Springer Series on Environmental Management. Retrieved from. <https://link.springer.com/book/10.1007%2F978-3-319-46709-2>.
- Asner, G.P., Heidebrecht, K.B., 2002. Spectral unmixing of vegetation, soil and dry carbon cover in arid regions: comparing multispectral and hyperspectral observations. *Int. J. Remote Sens.* 23, 3939–3958.
- Barger, N.N., Archer, S.R., Campbell, J.L., Huang, C.Y., Morton, J.A., Knapp, A.K., 2011. Woody plant proliferation in north American drylands: a synthesis of impacts on ecosystem carbon balance. *J. Geophys. Res.-Biogeosci.* 116 (G4).
- Bork, E., Su, J., 2007. Integrating LIDAR data and multispectral imagery for enhanced classification of rangeland vegetation: a meta analysis. *Remote Sens. Environ.* 111, 11–24.
- Bradford, J.B., Munson, S.M., Duniway, M.C., 2019. In: Gibson, D., Newman, J. (Eds.), *Assessing rangeland health under climate variability and change*. Pages 293–309 in: *grasslands and climate change*. Cambridge university press, Cambridge.
- Breiman, L., 1984. *Classification and regression trees*. Routledge, New York. <https://doi.org/10.1201/9781315139470>.
- Breshears, D.D., Whicker, J.J., Johansen, M.P., Pinder, J.E., 2003. Wind and water erosion and transport in semi-arid shrubland, grassland and forest ecosystems: quantifying dominance of horizontal wind-driven transport. *Earth Surf. Process. Landf.* 28 (11), 1189–1209.
- Brown, D.J., Shepherd, K.D., Walsh, M.G., Mays, M.D., Reinsch, T.G., 2006. Global soil characterization with VNIR diffuse reflectance spectroscopy. *Geoderma* 132 (3–4), 273–290.
- Browning, D.M., Archer, S.R., Asner, G.P., McClaran, M.P., Wessman, C.A., 2008. Woody plants in grasslands: post-encroachment stand dynamics. *Ecol. Appl.* 18, 928–944.
- Buscombe, D., Ritchie, A., 2018. Landscape classification with deep neural networks. *Geosciences* 8, 244.
- Colomina, I., Molina, P., 2014. Unmanned aerial systems for photogrammetry and remote sensing: a review. *ISPRS J. Photogramm. Remote Sens.* 92, 79–97.
- Congalton, R.G., Green, K., 2002. *Assessing the Accuracy of Remotely Sensed Data: Principles and Practices*. CRC press.
- Crucil, G., Castaldi, F., Aldana-Jague, E., van Wesemael, B., Macdonald, A., Van Oost, K., 2019. Assessing the performance of UAS-compatible multispectral and hyperspectral sensors for soil organic carbon prediction. *Sustainability* 11 (7).
- Cunliffe, A.M., Brazier, R.E., Anderson, K., 2016a. Ultra-fine grain landscape-scale quantification of dryland vegetation structure with drone-acquired structure-from-motion photogrammetry. *Remote Sens. Environ.* 183, 129–143.
- Cunliffe, A.M., Puttock, A.K., Turnbull, L., Wainwright, J., Brazier, R.E., 2016b. Dryland, calcareous soils store (and lose) significant quantities of near-surface organic carbon. *J. Geophys. Res.-Earth* 121 (4), 684–702.
- Dukes, D., Gonzales, H.B., Ravi, S., Grandstaff, D.E., Van Pelt, R.S., Li, J., Wang, G., Sankey, J.B., 2018. Quantifying postfire aeolian sediment transport using rare earth element tracers. *J. Geophys. Res.-Biogeosci.* 123 (1), 288–299.
- Duniway, M.C., Karl, J.W., Schrader, S., Baquera, N., Herrick, J.E., 2012. Rangeland and pasture monitoring: an approach to interpretation of high-resolution imagery focused on observer calibration for repeatability. *Environ. Monit. Assess.* 184 (6), 3789–3804.
- Eitel, J.U., Williams, C.J., Vierling, L.A., Al-Hamdan, O.Z., Pierson, F.B., 2011. Suitability of terrestrial laser scanning for studying surface roughness effects on concentrated flow erosion processes in rangelands. *Catena* 87 (3), 398–407.
- Elkind, K., Sankey, T.T., Munson, S.M., Aslan, C.E., 2019. Invasive buffelgrass detection using high-resolution satellite and UAV imagery on Google earth engine. *Remote Sens. Ecol. Conserv.* <https://doi.org/10.1002/rse2.116>.
- Foody, G., 2002. Status of land cover classification accuracy assessment. *Remote Sens. Environ.* 80, 185–201.
- Gholizadeh, H., Gamon, J.A., Townsend, P.A., Zygierbaum, A.I., Helzer, C.J., Hmimina, G.Y., Yu, R., Moore, R.M., Schweiger, A.K., Cavender-Bares, J., 2019. Detecting prairie biodiversity with airborne remote sensing. *Remote Sens. Environ.* 221, 38–49.
- Giglio, L., Boschetti, L., Roy, D.P., Humber, M.L., Justice, C.O., 2018. The collection 6 MODIS burned area mapping algorithm and product, *remote Sens. Environ.* 217, 72–85.
- Gillan, J.K., Karl, J.W., Duniway, M., Elaksher, A., 2014. Modeling vegetation heights from high resolution stereo aerial photography: an application for broad-scale rangeland monitoring. *J. Environ. Manag.* 144, 226–235.
- Gillan, J.K., Karl, J.W., Barger, N.N., Elaksher, A., Duniway, M.C., 2016. Spatially explicit rangeland erosion monitoring using high-resolution digital aerial imagery. *Rangel. Ecol. Manag.* 69, 95–107.
- Glenn, N.F., Streutker, D.R., Chadwick, D.J., Thackray, G.D., Dorsch, S.J., 2006. Analysis of LIDAR-derived topographic information for characterizing and differentiating landslide morphology and activity. *Geomorphology* 73, 131–148.
- Gonzales, H.B., Ravi, S., Li, J., Sankey, J.B., 2018. Ecohydrological implications of aeolian sediment trapping by sparse vegetation in drylands. *Ecohydrology* 11 (7).
- Grover, H.D., Musick, B., 1990. Shrubland encroachment in southern New Mexico, USA: an analysis of desertification processes in the American southwest. *Clim. Chang.* 17, 305–330.
- Hawbaker, T.J., Zhu, Z., 2012. Projected future wildland fires and emissions for the Western United States, in *Baseline and Projected Future Carbon Storage and Greenhouse-Gas Fluxes in Ecosystems of the Western United States*, edited by Z. Zhiliang and B. C. Reed. U.S. Geol. Surv. Prof. Pap., 1797 chap. 8, 12 pp. Available at. <https://pubs.usgs.gov/pp/1797/>.
- Holechek, J.L., Pieper, R.D., Herbel, C.H., 2011. *Range Management: Principles and Practices*, 6th edn. New York, Pearson Education, Inc.
- Houghton, R.A., 2003. Why are estimates of the terrestrial carbon balance so different? *Glob. Chang. Biol.* 9, 500–509.
- Huang, C., Asner, G.P., Martin, R., Barger, N., Neff, J., 2009. Multiscale analysis of tree cover and aboveground carbon stocks in pinyon-juniper woodlands. *Ecol. Appl.* 19, 668–681.
- Huenneke, L.F., Anderson, J.P., Remmenga, M., Schlesinger, W.H., 2002. Desertification alters patterns of aboveground net primary production in Chihuahuan ecosystems. *Glob. Chang. Biol.* 8, 247–264.
- Hunt Jr., E.R., Everitt, J.H., Ritchie, J.C., Moran, M.S., Booth, D.T., Anderson, G.L., Clark, P.E., Seyfried, M.S., 2003. Applications and research using remote sensing for rangeland management. *Photogramm. Eng. Remote. Sens.* 69, 675–693.
- Kasprak, A., Bransky, N., Sankey, J.B., Caster, J., Sankey, T.T., 2019. The effects of topographic surveying technique and data resolution on the detection and interpretation of geomorphic change. *Geomorphology* 330, 1–15.
- Kattenborn, T., Lopatin, J., Förster, M., Braun, A.C., Fassnacht, F.E., 2019. UAV data as alternative to field sampling to map woody invasive species based on combined Sentinel-1 and Sentinel-2 data. *Remote Sens. Environ.* 227, 61–73.
- Knapp, A.K., Briggs, J.M., Collins, S.L., Archer, S.R., Bret-Harte, M.S., Ewers, B.E., Peters, D.P., Young, D.R., Shaver, G.R., Pendall, E., Cleary, M.B., 2008. Shrub encroachment in north American grasslands: shifts in growth form dominance alters control of ecosystem carbon inputs. *Glob. Chang. Biol.* 14, 615–623.
- Kokaly, R.F., Rockwell, B.W., Haire, S.L., King, T.V., 2007. Characterization of post-fire surface cover, soils, and burn severity at the Cerro Grande fire, New Mexico, using hyperspectral and multispectral remote sensing. *Remote Sens. Environ.* 106, 305–325.
- Laliberte, A.S., Goforth, M.A., Steele, C.M., Rango, A., 2011. Multispectral remote sensing from unmanned aircraft: image processing workflows and applications for rangeland environments. *Remote Sens.* 3 (11), 2529–2551.
- Lawrence, R.L., Wright, A., 2001. Rule-based classification systems using classification and regression tree (CART) analysis. *Photogramm. Eng. Remote. Sens.* 67 (10), 1137–1142.
- Lee, J.A., 1991a. The role of desert shrub size and spacing on wind profile parameters. *Phys. Geogr.* 12 (1), 72–89.
- Lee, J.A., 1991b. Near-surface wind flow around desert shrubs. *Phys. Geogr.* 12 (2), 140–146.
- Li, J., Okin, G.S., Alvarez, L., Epstein, H., 2007. Quantitative effects of vegetation cover on wind erosion and soil nutrient loss in a desert grassland of southern New Mexico. *USA. Biogeochem.* 85 (3), 317–332.
- Li, J., Okin, G.S., Alvarez, L., Epstein, H., 2008. Effects of wind erosion on the spatial heterogeneity of soil nutrients in two desert grassland communities. *Biogeochem.* 88 (1), 73–88.
- Lopatin, J., Fassnacht, F.E., Kattenborn, T., Schmidlein, S., 2017. Mapping plant species in mixed grassland communities using close range imaging spectroscopy. *Remote Sens. Environ.* 201, 12–23.
- Massey, R., Sankey, T., Yadav, K., Congalton, R., Tilton, J., 2018. Integrating cloud-based workflows in continental-scale cropland extent classification. *Remote Sens. Environ.* 219, 162–179.
- McGlynn, I.O., Okin, G.S., 2006. Characterization of shrub distribution using high spatial resolution remote sensing: ecosystem implications for a former Chihuahuan Desert grassland. *Remote Sens. Environ.* 101 (4), 554–566.
- Miesel, J.R., Kolka, R., Townsend, P., 2018. Wildfire and fire severity effects on post-fire carbon and nitrogen cycling in forest soil (Project NC-EM-F-14-1). In: Potter, Kevin M., Conkling, Barbara L. (Eds.), *Forest health monitoring: national status, trends, and analysis 2017*. General Technical Report SRS-233. US Department of Agriculture, Forest Service, Southern Research Station, Asheville, NC, pp. 151–156.
- Millennium Ecosystem Assessment, 2005. *Ecosystems and Human Well-Being: Desertification Synthesis*. Island Press, Washington, DC, World Resources Institute.
- Miller, R.F., Svejcar, T.J., Rose, J.A., 2000. Impacts of western juniper on plant community composition and structure. *J. Range Manag.* 53, 574–585.
- Mitchell, J.J., Glenn, N.F., Sankey, T.T., Derryberry, D.R., Germino, M.J., 2012. Remote sensing of sagebrush canopy nitrogen. *Remote Sens. Environ.* 124, 217–223.
- Munson, S.M., Muldavin, E.H., Belnap, J., Peters, D.P., Anderson, J.P., Reiser, M.H., Gallo, K., Melgoza-Castillo, A., Herrick, J.E., Christiansen, T.A., 2013. Regional signatures of plant response to drought and elevated temperature across a desert ecosystem. *Ecology* 94 (9), 2030–2041.
- Munson, S.M., Sankey, T.T., Xian, G., Villarreal, M.L., Homer, C.G., 2016. Decadal shifts in grass and woody plant cover are driven by prolonged drying and modified by topo-edaphic properties. *Ecol. Appl.* 26 (8), 2480–2494.
- Nocita, M., Stevens, A., van Wesemael, B., Aitkenhead, M., Bachmann, M., Barthès, B., Dor, E.B., Brown, D.J., Clairrotte, M., Csorba, A., Dardenne, P., 2015. Soil spectroscopy: an alternative to wet chemistry for soil monitoring. In: *Advances in agronomy*, Vol. 132. Academic Press, pp. 139–159.
- Okin, G.S., 2008. A new model for wind erosion in the presence of vegetation. *J. Geophys. Res.* 113, F02S10. <https://doi.org/10.1029/2007JF000758>.
- Okin, G.S., Gillette, D.A., 2001. Distribution of vegetation in wind-dominated landscapes: implications for wind erosion modeling and landscape processes. *J. Geophys. Res.-Atmos.* 106 (D9), 9673–9683.
- Okin, G.S., Roberts, D.A., Murray, B., Okin, W., 2001. Practical limits on hyperspectral vegetation discrimination in arid and semiarid environments. *Remote Sens. Environ.* 77, 212–225.
- Olofsson, P., Foody, G.M., Herold, M., Stehman, S.V., Woodcock, C.E., Wulder, M.A., 2014. Good practices for estimating area and assessing accuracy of land change. *Remote Sensing of Environment* 148, 42–57.
- Pacala, S.W., Hurtt, G.C., 2001. Consistent land- and atmosphere-based U.S. carbon sink estimates. *Science* 292, 2316–2319.
- Peters, D.P., Yao, J., Sala, O.E., Anderson, J.P., 2012. Directional climate change and potential reversal of desertification in arid and semiarid ecosystems. *Glob. Chang. Biol.* 18 (1), 151–163.



- Puttock, A., Dungait, J.A., Macleod, C.J., Bol, R., Brazier, R.E., 2014. Woody plant encroachment into grasslands leads to accelerated erosion of previously stable organic carbon from dryland soils. *J. Geophys. Res.-Biogeosci.* 119 (12), 2345–2357.
- Ramsey, R.D., Dennis, D.L., McGinty, C., 2004. Evaluating the use of Landsat 30 m enhanced thematic mapper to monitor vegetation cover in shrub-steppe environments. *Geocarto Int.* 19, 39–47.
- Rau, B.M., Johnson, D.W., Blank, R.R., Chambers, J.C., 2009. Soil carbon and nitrogen in a Great Basin pinyon-juniper woodland: influence of vegetation, burning, and time. *J. Arid Env* 73, 472–479.
- Rau, B.M., Johnson, D.W., Blank, R.R., Tausch, R.J., Roundy, B.A., Miller, R.F., Caldwell, T.G., Lucchesi, A., 2011. Woodland expansion's influence on belowground carbon and nitrogen in the Great Basin, U.S., *J. Arid Env* 75, 827–835.
- Ravi, S., D'Odorico, P., 2009. Post-fire resource redistribution and fertility island dynamics in shrub encroached desert grasslands: a modeling approach. *Landsc. Ecol.* 24 (3), 325–335.
- Ravi, S., D'Odorico, P., Wang, L., White, C.S., Okin, G.S., Macko, S.A., Collins, S.L., 2009. Post-fire resource redistribution in desert grasslands: a possible negative feedback on land degradation. *Ecosystems* 12 (3), 434–444.
- Ravi, S., Breshears, D.D., Huxman, T.E., D'Odorico, P., 2010. Land degradation in drylands: interactions among hydrologic-aolian erosion and vegetation dynamics. *Geomorphology* 116 (3–4), 236–245.
- Ravi, S., Gonzales, H.B., Buynevich, I.V., Li, J., Sankey, J.B., Dukes, D., Wang, G., 2019. On the development of a magnetic susceptibility-based tracer for aeolian sediment transport research. *Earth Surf. Process. Landf.* 44 (2), 672–678.
- RIEGL, 2017. VZ-1000 Data Sheet Version 2017-06-14. [http://www.riegl.com/uploads/t\\_x\\_pxpriegl/downloads/DataSheet\\_VZ-1000\\_2017-06-14.pdf](http://www.riegl.com/uploads/t_x_pxpriegl/downloads/DataSheet_VZ-1000_2017-06-14.pdf). (Accessed 25 September 2020).
- Romme, W.H., Allen, C.D., Bailey, J.D., Baker, W.L., Bestelmeyer, B.T., Brown, P.M., Eisenhart, K.E., Floyd, M.L., Huffman, D.W., Jacobs, B.F., Miller, R.F., Muldavin, E. H., Swetnam, T.W., Tausch, R.J., Weisberg, P.J., 2009. Historical and modern disturbance regimes, stand structures, and landscape dynamics in pinyon-juniper vegetation of the western United States. *Rangel. Ecol. Manag.* 62, 203–222.
- Sankey, T.T., Germino, M.J., 2008. Assessment of juniper encroachment with the use of satellite imagery and geospatial data. *Rangel. Ecol. Manag.* 61, 412–418.
- Sankey, J.B., Brown, D.J., Bernard, M.L., Lawrence, R.L., 2008. Comparing local vs. global visible and near-infrared (VisNIR) diffuse reflectance spectroscopy (DRS) calibrations for the prediction of soil clay, organic C and inorganic C. *Geoderma* 148, 149–158.
- Sankey, J.B., Germino, M.J., Glenn, N.F., 2009. Aeolian sediment transport following wildfire in sagebrush steppe. *J. Arid Environ.* 73 (10), 912–919.
- Sankey, J.B., Ravi, S., Wallace, C.S., Webb, R.H., Huxman, T.E., 2012a. Quantifying soil surface change in degraded drylands: shrub encroachment and effects of fire and vegetation removal in a desert grassland. *J. Geophys. Res.-Biogeosci.* 117 (G2).
- Sankey, J.B., Germino, M.J., Sankey, T.T., Hoover, A.N., 2012b. Fire effects on the spatial patterning of soil properties in sagebrush steppe, USA: a meta-analysis. *Int. J. Wildland Fire* 21 (5), 545–556.
- Sankey, T.T., Moffet, C., Weber, K., 2008b. Postfire recovery of sagebrush communities: assessment using SPOT-5 and very large-scale aerial imagery. *Rangel. Ecol. Manag.* 61, 598–604.
- Sankey, T., Shrestha, R., Sankey, J.B., Hardegre, S., Strand, E., 2013. Lidar-derived estimate and uncertainty of carbon sink in successional phases of woody encroachment. *J. Geophys. Res.-Biogeosci.* 118 (3), 1144–1155.
- Sankey, T., Dickson, B., Sessie, S., Wang, O., Olsson, A., Zachmann, L., 2014. WorldView-2 high spatial resolution improves desert invasive plant detection Photogramm. Engineer. *Remote Sens.* 80 (9), 885–893.
- Sankey, T., Donager, J., McVay, J., Sankey, J.B., 2017a. UAV lidar and hyperspectral fusion for forest monitoring in the southwestern USA. *Remote Sens. Environ.* 195, 30–43.
- Sankey, T.T., McVay, J., Swetnam, T., McClaran, M.P., Heilman, P., Nicols, M., 2017b. UAV lidar and hyperspectral fusion: a new research tool for biogeoscience. *Remote Sens. Ecol. Conserv.* 4, 1–12.
- Sankey, T., Massey, R., Yadav, K., Congalton, R., Tilton, J., 2018. Post-socialist cropland changes and abandonment in Mongolia. *Land Degrad. Dev.* 29 (9), 2808–2821.
- Sankey, T.T., Leonard, J.M., Moore, M.M., 2019. Unmanned aerial vehicle—Based rangeland monitoring: examining a century of vegetation changes. *Rangeland Ecology and Management* 72 (5), 858–863.
- Schlesinger, W.H., Reynolds, J.F., Cunningham, G.L., Huenneke, L.F., Jarrell, W.M., Virginia, R.A., Whitford, W.G., 1990. Biological feedbacks in global desertification. *Science (Washington)* 247 (4946), 1043–1048.
- Schlesinger, W.H., Raikes, J.A., Hartley, A.E., Cross, A.F., 1996. On the spatial pattern of soil nutrients in desert ecosystems. *Ecology* 77 (2), 364–374.
- Scholes, R.J., Archer, S.R., 1997. Tree-grass interactions in savannas. *Annu. Rev. Ecol. Syst.* 28, 517–544.
- Schweiger, A., Cavender-Bare, J., Townsend, P., Hobbie, S., Madritch, M., Wang, R., Tilman, D., Gamon, J., 2018. Plant spectral diversity integrates functional and phylogenetic components of biodiversity and predicts ecosystem function. *Nat. Ecol. Evol.* 2, 976–982.
- Shin, P., Sankey, T., Moore, M., Thode, A., 2018. Evaluating unmanned aerial vehicle images for estimating Forest canopy fuels in a ponderosa pine stand. *Remote Sens.* 10 (8), 1266.
- Sivanpillai, R., Booth, D.T., 2008. Characterizing rangeland vegetation using Landsat and 1-mm VLSA data in Central Wyoming (USA). *Agrofor. Syst.* 73, 55–64.
- Solazzo, D., Sankey, J.B., Sankey, T.T., Munson, S.M., 2018. Mapping and measuring aeolian sand dunes with photogrammetry and LiDAR from unmanned aerial vehicles (UAV) and multispectral satellite imagery on the Paria plateau, AZ, USA. *Geomorphology* 319, 174–185.
- Strand, E.K., Vierling, L.A., Smith, A.M.S., Bunting, S.C., 2008. Net changes in aboveground woody carbon stock in western juniper woodlands, 1946–1998. *J. Geophys. Res.* 113, G01013 <https://doi.org/10.1029/2007JG000544>.
- Streutker, D.R., Glenn, N.F., 2006. LiDAR measurement of sagebrush steppe vegetation heights. *Remote Sens. Environ.* 102, 135–145.
- Therneau, T., Atkinson, B., 2019. Rpart: recursive partitioning and regression trees. R package version 4, 1–15. <https://CRAN.R-project.org/package=rpart>.
- Thomas, R.W., Ustin, S.L., 1987. Discriminating semiarid vegetation using airborne imaging spectrometer data: a preliminary assessment. *Remote Sensing of Environment* 23 (2), 273–290.
- Throop, H.L., Lajtha, K., Kramer, M., 2013. Density fractionation and  $^{13}\text{C}$  reveal changes in soil carbon following woody encroachment in a desert ecosystem. *Biogeochemistry* 112 (1–3), 409–422.
- Turner, W., 2014. Sensing biodiversity. *Science* 346 (6207), 301–302.
- UNCCD, 1994. United Nations convention to combat desertification in countries experiencing serious drought and/or desertification, particularly in Africa. A/AC.241/27, (September), pp. 1–58 accessed online. <http://www.unccd.int/convention/menu.php>, 15 January, 2017.
- Van Auken, O.W., 2000. Shrub invasions of north American semiarid grasslands. *Annu. Rev. Ecol. Syst.* 31 (1), 197–215.
- Van Cleemput, E., Vanierschot, L., Fernández-Castilla, B., Honnay, O., Somers, B., 2018. The functional characterization of grass-and shrubland ecosystems using hyperspectral remote sensing: trends, accuracy and moderating variables. *Remote Sens. Environ.* 209, 747–763.
- Van Wilgen, B., Trollope, W., 2003. Fire as a driver of ecosystem variability. In: Johan, T. T., Kevin, H.R., Harry, C.B. (Eds.), *The Kruger Experience: Ecology and Management of Savanna Heterogeneity*. Island Press, Washington, DC, pp. 149–170.
- Waiser, T.H., Morgan, C.L., Brown, D.J., Hallmark, C.T., 2007. In situ characterization of soil clay content with visible near-infrared diffuse reflectance spectroscopy. *Soil Sci. Soc. Am. J.* 71 (2), 389–396.
- Wang, G., Li, J., Ravi, S., Dukes, D., Gonzales, H.B., Sankey, J.B., 2019a. Post-fire redistribution of soil carbon and nitrogen at a grassland-Shrubland ecotone. *Ecosystems* 22 (1), 174–188.
- Wang, G., Li, J., Ravi, S., Theiling, B.P., Sankey, J.B., 2019b. Fire changes the spatial distribution and sources of soil organic carbon in a grassland-shrubland transition zone. *Plant Soil* 435 (1–2), 309–321.
- Washington-Allen, R.A., West, N.E., Ramsey, R.D., Efromymson, R.A., 2006. A protocol for retrospective remote sensing-based ecological monitoring of rangelands. *Rangeland Ecol. Manag.* 59 (1), 19–29.
- White, C.S., 2011. Homogenization of the soil surface following fire in semiarid grasslands. *Rangeland Ecol. Manag.* 64 (4), 414–418.
- White, C.S., Pendleton, R.L., Pendleton, B.K., 2006. Response of two semiarid grasslands to a second fire application. *Rangeland Ecol. Manag.* 59 (1), 98–106.
- Zhang, N., Zhang, X., Yang, G., Zhu, C., Huo, L., Feng, H., 2019. Assessment of defoliation during the *Dendrolimus tabulaeformis* Tsai et Liu disaster outbreak using UAV-based hyperspectral images. *Remote Sensing of Environment* 217, 323–339. <https://doi.org/10.1016/j.rse.2018.08.024>.
- Xian, G., Homer, C., Rigge, M., Shi, H., Meyer, D., 2015. Characterization of shrubland ecosystem components as continuous fields in the Northwest United States. *Remote Sens. Environ.* 168, 286–300.